CHALMERS
UNIVERSITY OF TECHNOLOGY

Virtual development of H2 gas compressor and H2 storage system for HPDI engines

Compressed H2 storage systems towards environmentally-friendly and efficient heavy-duty vehicle engines development

Master's thesis in Complex Adaptive Systems

IOANNIS KAKKOS

DEPARTMENT OF MECHANICS AND MARITIME SCIENCES

CHALMERS UNIVERSITY OF TECHNOLOGY
Göteborg, Sweden 2023
www.chalmers.se

Master's thesis 2023

Virtual development of H2 gas compressor and H2 storage system for HPDI engines

Compressed H2 storage systems towards environmentally-friendly and efficient heavy-duty vehicle engines development

IOANNIS KAKKOS

CHALMERS
UNIVERSITY OF TECHNOLOGY

Department of Mechanics and maritime sciences
Chalmers University of Technology
Göteborg, Sweden 2023

Virtual development of H2 gas compressor and H2 storage system for HPDI engines
Compressed H2 storage systems towards environmentally-friendly and efficient heavy-duty vehicle engines development
IOANNIS KAKKOS

Supervisor: Rafig Babayev, Volvo Group Trucks Technology
Examiner: Lucien Koopmans, Department of Mechanics and Maritime Sciences

Master's Thesis 2023
Department of Mechanics and Maritime Sciences
Chalmers University of Technology
SE-412 96 Göteborg
Telephone +46 31 772 1000

Typeset in LaTeX
Printed by Chalmers Reproservice
Göteborg, Sweden 2023

Virtual development of H2 gas compressor and H2 storage system for HPDI engines
Compressed H2 storage systems towards environmentally-friendly and efficient heavy-duty vehicle engines development
Ioannis Kakkos
Department of Mechanics and Maritime Sciences
Chalmers University of Technology

Abstract

Transition to alternative fuel sources constitutes a necessity for most large-scale operating industries. Although fuel-cell electric vehicles have undergone extensive research, there is an area in hydrogen potential that is yet to be thoroughly investigated. Companies are investigating hydrogen use in internal combustion engines, employing configurations such as diffusion combustion of a hydrogen spray, among others, as an alternative to diesel fuel with the scope of incorporating this technology in their heavy-duty truck fleet. This thesis performed under Volvo Group AB deals with the concept of HPDI H2 engines, mainly focusing on the storage tanks and their discharge, as well as the compressor. Simulations were performed on Matlab's Simulink, where a model was built and incorporated with Volvo's in-house simulation platform. Real gas assumption was implemented for hydrogen because of very high storage pressures of up to 700 bar. On these pressure levels the contribution of compressibility in the real-gas equation becomes very important. During tank discharge, it is important to simulate adiabatic and isothermal discharging since it makes a great difference on the range achieved by the vehicle. Another important parameter is payload which directly affects fuel consumption and reduces driving range. Apart from reducing the driving range, it was found that payload significantly increases the compressor power consumption.

Keywords: HPDI, CI, non-premixed, diffusion combustion, heavy-duty truck, tank discharge, tank deployment

Acknowledgements

Performing this thesis in the course of a year has been a truly valuable experience with difficulties and lessons to be learned in the way. I would like to express my gratitude to my supervisor in Volvo Group, Rafig Babayev, for supporting me throughout this whole process and having countless of interesting conversations which helped me overcome and understand the issues connected with this project. I would especially like to express my appreciation and gratitude for my examiners, Mats Andersson and Lucien Koopmans for assisting me and raising so many precious points along the way. Their input helped me understand the basis of my thesis and shaped the form of this project.
I would also like to say thanks to my group members in Volvo Group, as well as the various engineers I had the chance to interact with within the company. A fresh way of thinking is very valuable when you have been stuck for long periods of time. Last but not least, I have to express my deepest gratitude to my family, my parents and my sister, and my friends for their consistent support and patience during this year. Their help is invaluable.

Ioannis Kakkos, Göteborg, July 2023

List of Acronyms

The list of acronyms that have been used throughout this thesis listed in alphabetical order:

BWR	Bennedict-Webb-Rubin
CI	Compression Ignition
CFRP	Carbon Fiber Reinforced Plastic
DC	drive-cycle
EOS	Equation of State
GCW	Gross Combination Weight
GSP	Global Simulations Platform
HHV	Higher Heating Value
HPDI	High Pressure Direct Injection
HSS	Hydrogen Storage System
ICE	Internal Combustion Engine
JT	Joule-Thomson
LHV	Lower Heating Value
LNG	Liquefied Natural Gas
NOx	Nitrogen Oxides
RMS	Root Mean Square
SRK	Soave-Redlich-Kwong

Nomenclature

Below is the nomenclature of indices, sets, parameters, and variables that have been used throughout this thesis.

Greek letters

α	thermal diffusivity $[m^2/s]$
α_{const}	constant coefficient [K/Pa]
β	thermal expansion coefficient [1/K]
μ	dynamic viscosity $[Pa \cdot s]$
μ_{JT}	Joule-Thomson coefficient [-]
ρ	density $[kg/m^3]$
υ	kinematic viscosity $[m^2/s]$
ω	eccentric factor [-]

Indices

0	reference value
amb	index referring to ambient conditions
C	critical value
g	index for gas
i	index for inner vessel wall
JT	Joule-Thomson
o	index for outer vessel wall
r	ratio
s	surface
w	wall
wi	index referring to inner wall

wo	index referring to outer wall

Parameters

∂P	partial differential of pressure
∂T	partial differential of temperature
C	Sutherland's constant for hydrogen
D	cylindrical vessel diameter [m]
dH	enthalpy derivative
dQ	heat transfer derivative
dt	time interval
dT_g	gas temperature derivative
dU	internal energy derivative
g	gravitational acceleration $[m/s^2]$
L	characteristic length [m]
P_C	critical pressure [bar]
R	universal gas constant [J/K/mol]
T_C	critical temperature [K]

Variables

A	surface area $[m^2]$
c_v	specific heat capacity [J/kg/K]
h	convective heat transfer coefficient $[W/m^2/K]$
k	thermal conductivity [W/m/K]
m_g	mass of gas [kg]
$\dot{m}_g$	mass flow rate of gas [kg/s]
Nu	Nusselt number [-]
p_g	gas pressure [bar]
$\dot{Q}$	heat transfer rate [W]
R_{spec}	specific gas constant [J/kg/K]
Ra	Rayleigh number [-]
T_r	temperature ratio
v_g	specific volume of gas $[m^3/kg]$

z	compressibility

Contents

List of Figures

List of Tables

1

Introduction

1.1 Background

Hydrogen energy production and utilization is highly considered in modern society because it constitutes a renewable and potentially pollution free fuel. Nowadays, hydrogen usage in ICEs is receiving increasing attention, especially in heavy-duty vehicles. The reason is related to the actual properties of hydrogen, as well as technological advancement. First and foremost, hydrogen constitutes a renewable energy source (RES) and its combustion produces zero carbon products. Modifying a significant percentage of existing heavy-duty truck engines, which run on diesel, so that they run on hydrogen, would have a strong impact on carbon emissions and climate change and research is beginning to orient towards this field [11], [1] and [12]. This substitution of pre-existing ICEs in order to incorporate changes that allow for hydrogen combustion is a sustainable choice since it involves fitting the already mature design of ICEs in order to account for hydrogen combustion. There has been increasing attention and research towards offsetting the environmental impact of hydrocarbon use in the transport industry, as well as exploring the prospects of producing hydrogen in a sustainable manner. Reportedly, the production of 1 tonne of hydrogen with conventional methods might produce up to 5 tonnes of CO_2 as a byproduct [1]. This issue can be countered by using RES to produce hydrogen. Achieving production through RES is a sign of technological maturity in hydrogen production technology and is very important for the future development of hydrogen combustion engines [12]. Fossil fuel reserves and climate change dictate the need for such a transition, among other reasons. The current legislation concerning sustainable development targets also provide important background that necessitate such measures to be taken [13] and [14]. The hydrogen fuel cycle is the process through which hydrogen is produced and it consists of an environmentally clean production process, since the reactant and the product can, potentially, both be plain water [5]. The latter is contingent on water being used to produce hydrogen, through electrolysis. A 2010 study investigating the prospects and challenges of hydrogen production, reports that only a small fraction of hydrogen produced globally is based on water as a raw material, as shown in Figure 1.2 [1]. The prevailing material used to produce hydrogen, at the time this study was released, was natural gas followed by petroleum and coal. The shift towards water-based hydrogen production is an essential step to decarbonize the production method, with lowering the production cost constituting an indispensable part of it as shown in Figure 1.1. Another requirement towards the decarbonization process is to increase the participation of

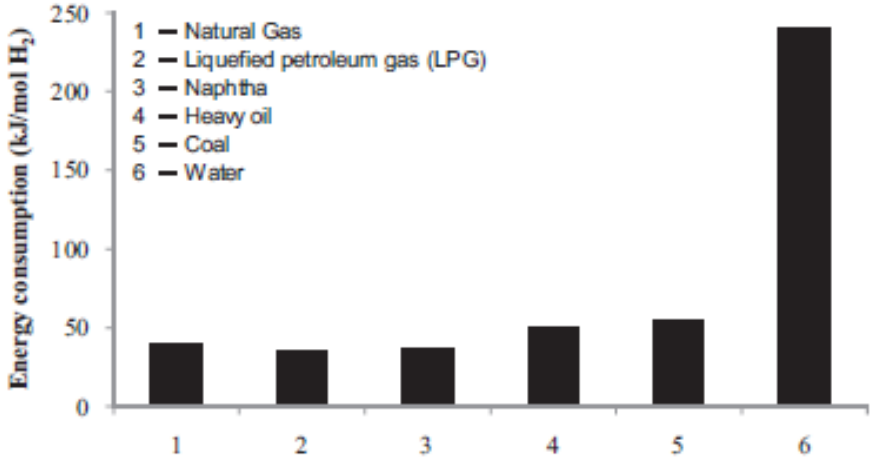

Figure 1.1: Hydrogen production energy cost [1]

RES to produce hydrogen.

Certain aspects of gaseous hydrogen constitute a very attractive choice in ICEs. The calorific value of hydrogen is almost three times higher than that of diesel, 120 MJ/kg versus 42 MJ/kg, respectively, so hydrogen contains significantly higher amounts of energy per unit mass, compared to diesel. On the other hand, hydrogen turns out to be very costly to transfer, since it contains less than three times the energy diesel contains per unit volume. The relevant values for hydrogen and diesel are 10.8 MJ/m^3 and 36 MJ/m^3, respectively. Thus, the storage system of hydrogen-driven vehicles has to be multiple times larger than that of diesel-driven vehicles, in order to carry equivalent amount of energy. The preceding statement is true for HPDI engines, among other, using gaseous hydrogen in a non-premixed injection environment to achieve power production for on-board applications. Another important component of systems that require high pressure injection is a compressor suitable to provide the necessary levels of pressure to the engine when the tanks have discharged below a specific point. This compressor or gas booster is also an important part of the work of this thesis. The properties mentioned above concerning gaseous hydrogen, as well as other fuels, are provided in Figure 1.3. HPDI LNG engines, such as the one that has been extensively developed by Westport, are also a strong candidate for hydrogen applicability [15]. Such diffusion combustion engines have been thoroughly investigated and used with natural gas. The HPDI technology might easily be adapted to fit the needs of a hydrogen-fuelled engine [16]. Regarding technological advancement around hydrogen fuel, there are certain barriers that have to be surpassed. Storage tanks have undergone extensive development and can now be used to store gaseous hydrogen in very high pressures. Those are type IV tanks and they have a nominal working pressure of 700 bar [17]. Those tanks consist of an internal aluminum layer, called liner, and a significantly thicker external carbon-fibre reinforced plastic (CFRP) layer. The combination of those two layers offers high structural stability and low tank weight at high levels of pressure.

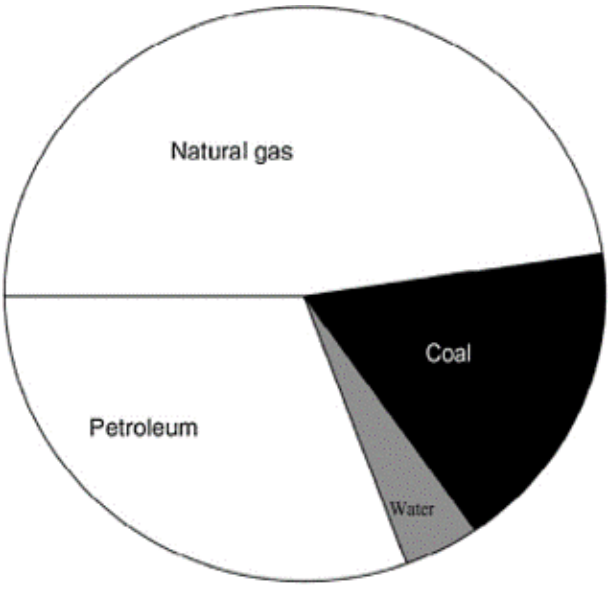

Figure 1.2: Relative quantities of raw materials used to produce hydrogen [1]

1.2 Aim

This work aims to answer specific questions regarding the use of hydrogen in a non-premixed combustion ICE, focusing on the compressor and the delivery system in general. The general area of investigation is the hydrogen path from the tanks, where it is stored highly pressurized in gas form, to the engine. Specifically, this path involves the tanks, the piping system and losses that might involve, the compressor and perhaps some auxiliary equipment such as a cooler. The questions that arise are connected to the complexity of the interconnections participating in hydrogen's route. Such interconnected parts that contribute to delivering the fuel are the compressor, an expander, the cooling system, the tank valves and other auxiliary systems that might end up proving to be essential in the process of designing this model. This work targets to provide a clear view on how such a system might compare to the existing diesel ICEs in terms of thermal efficiency, and define limitations in the process of doing so. The main focus is directed towards defining the systems that are involved in the process of transferring hydrogen from tank to cylinder with the lowest losses possible for the system as a whole. An important area of investigation is the fact that, although hydrogen will be stored in a compressed state in the tanks at approximately 700 bar, the injection will take place at around 300 bar. This pressure difference amounts for a significant performance and efficiency loss, thus maximum tank utilization before reaching the target pressure of 300 bar is a key area of interest that shall be explored in this thesis. Thus, although a system that boosts hydrogen pressure before the injection might be necessary, the target is to develop suitable strategies that increase the overall system efficiency. Such control strategies should be able to handle different driving scenarios and provide an overall coverage of what a typical heavy-duty vehicle would encounter in the current road and driving conditions. The target is to achieve 90% tank utilization which means that 10% of initially stored fuel remains in the tanks by the end of any drive-cycle.

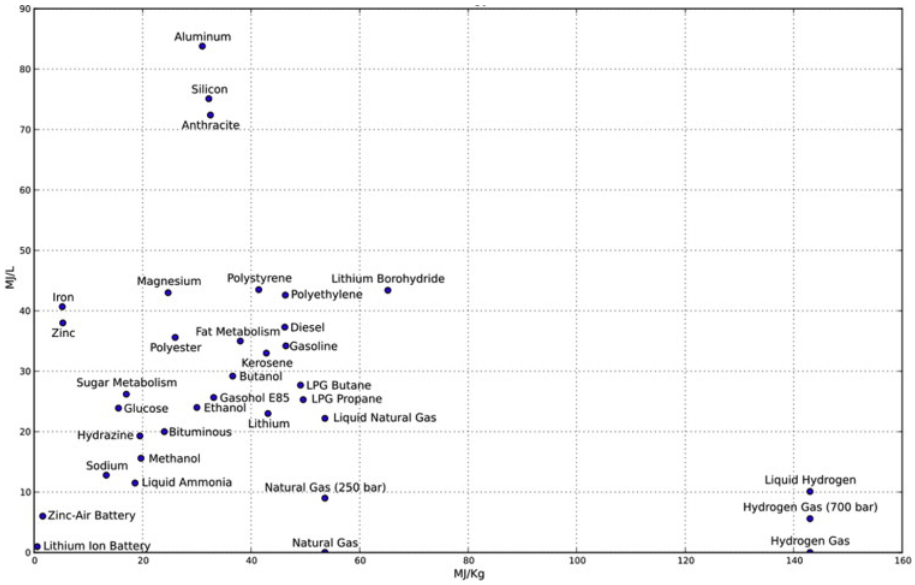

Figure 1.3: Energy density of various fuels [2]

1.3 Limitations

Same as pressure, temperature drops significantly during tank discharging and can reach levels close or well below the tanks lower temperature limit which is in turn translated into limitations in terms of capable driving range achieved by the vehicle. Of course, the system must be designed in a way that it never exceeds these limits. Another important aspect that requires modeling is the compressor or gas booster. This component is responsible for delivering the fuel to the cylinder injector in suitable pressure levels, depending on load. This task has two main dependencies, the first one is the hydrogen pressure in the vessels and the other is the discharging temperature, which is the gas temperature when it leaves the booster. There is a certain lower pressure limit from which the compressor would be able to compress, since the size of the compressor is an important property that should be taken into account for on-board applications. Temperature is mainly an issue related to the discharge state of the compressed hydrogen gas. The significance of the compressor discharge temperature lies onto the technology of the components that seal the moving parts of the reciprocating compressor as well as the lubricating medium. All these limitations and constraints have to be considered and the suggestion is for a realistic technical proposal to be able to define these limits connected with the potential of this configuration.

2
Theory

2.1 Thermodynamics

2.1.1 Tank discharging

In order to simulate the tanks, the 1^{st} Law of Thermodynamics was employed, as developed in (2.1). This differential equation provides the temperature profile of gaseous hydrogen, as a function of escaping mass rate $\dot{m}_g$, gas pressure p_g, specific volume υ_g and heat transfer rate $\dot{Q}_i$. The analytical calculation leading to (2.1) is provided in (A.1).

$$\frac{dU}{dt} = \frac{dH}{dt} - \frac{dQ}{dt} \Rightarrow \ldots \Rightarrow \boxed{\frac{dT_g}{dt} = \frac{1}{c_v(T)m_g}(\dot{m}_g p_g v_g - \dot{Q})} \tag{2.1}$$

The subject of this work is mainly connected to the discharging of tanks during normal operation of a heavy-duty vehicle rather than tank refill, which is another key area of investigation. This means that the heat transfer rate $\dot{Q}$ described in (2.1) is related to the temperature and mass drop in the tanks, due to conduction and convection that take place during discharge. An alternative expression for the temperature rate of change can be produced from the expression of (2.1). Equation (2.2) consists of a more useful tool since it is more straight-forward to model. It is apparent that the expression on (2.2) substitutes $p_g v_g$ with $zR_{spec}T_g$, making use of the Equation of State (EOS) for real gases, as depicted in (2.3). Equation (2.3) provides the pressure profile of gaseous hydrogen, once the temperature gradient has been estimated from (2.1).

$$\frac{dT_g}{dt} = \frac{1}{c_v(T)m_g}(\dot{m}_g z R_{spec} T_g - \dot{Q}_i) \tag{2.2}$$

$$pv = zRT \tag{2.3}$$

The newly introduced terms of z and R_{spec} correspond to compressibility and specific gas constant, respectively. The units of (2.2) are provided analytically in (2.4).

$$\begin{gathered}\frac{[K]}{[s]} = \frac{1}{\frac{[J]}{[kg][K]}[kg]}\left(\frac{[kg]}{[s]}[-]\frac{[J]}{[kg][K]}[K] - \frac{[J]}{[s]}\right) \Rightarrow \\ \frac{[K]}{[s]} = \frac{1}{\frac{[\cancel{J}]}{[\cancel{kg}][\mathbf{K}]}[\cancel{kg}]}\left(\frac{[\cancel{kg}]}{[\mathbf{s}]}[-]\frac{[\cancel{J}]}{[\cancel{kg}][\cancel{K}]}[K] - \frac{[\cancel{J}]}{[\mathbf{s}]}\right)\end{gathered} \tag{2.4}$$

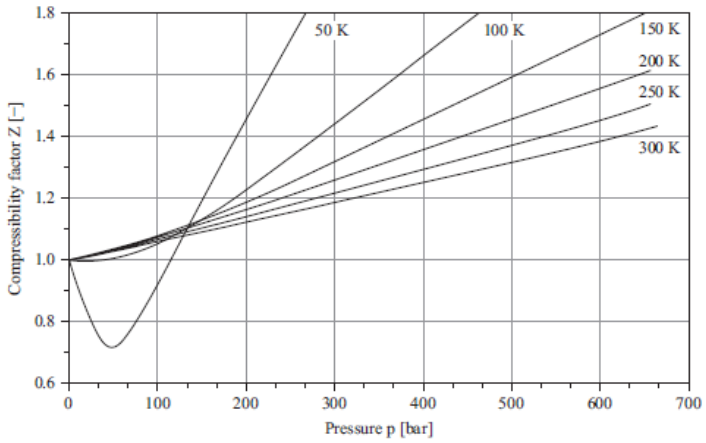

Figure 2.1: Hydrogen compressibility factor in relation to gas pressure and temperature [3]

At this point it should be noted that compressibility calculation is essential since this study involves high pressure gaseous hydrogen flow with a temperature profile variation during tank discharge. The dependency of compressibility on pressure and temperature is depicted in Figure 2.1. The compressibility effect becomes significant and therefore should be calculated in parallel with the rest of the quantities that govern the equation of state (EOS). The exact methodology used to do that is presented in the relevant subsection of this work.

The charged state of the tanks is considered to contain gaseous hydrogen at around 700 bar and, as the tanks discharge, apart from the pressure drop, they encounter a temperature drop as well. The specific calorific value, as expressed in the denominator of (2.2), was calculated as a function of temperature instead of using a constant value. The choice regarding the c_v calculation method is supported by a sensitivity analysis performed, which involved comparing a constant value of c_v as opposed to one calculated through NASA polynomials. As indicated in Figure 2.2, there is very slight deviation between the two estimated sets of values of specific calorific value, so the choice was based on the most accurate method of calculation, which is the one where c_v varies with temperature and is calculated through some experimentally produced coefficients, namely the NASA polynomials. Figure 2.2 deliberately presents the adiabatic process instead of the isothermal one. This is due to the fact that the adiabatic process produces more significant deviation between the two methods, since isothermal process assumes constant temperature during discharge, thus the results are identical in the two proposed methods for isothermal discharge process.

Mass m_g in the denominator of (2.2) refers to total hydrogen mass in the system and since this mass is leaving the system with a rate defined by the instantaneous consumption rate of the engine, the ratio as a whole exhibits an upward trend with time, considering that the rate of change for c_v is insignificant with respect to that of total mass.

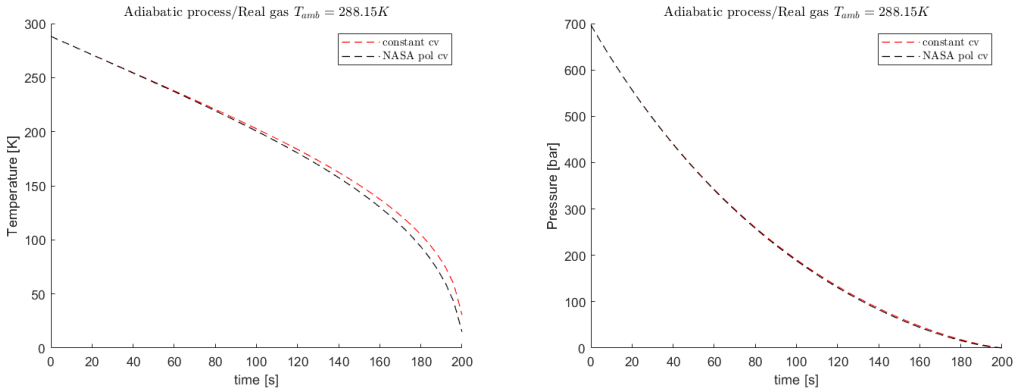

Figure 2.2: Temperature and pressure as a function of time while emptying the tank at a constant rate

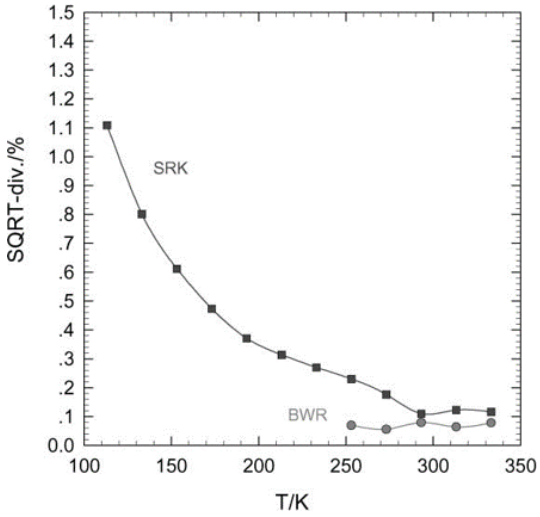

Figure 2.3: RMS deviation of compressibility equations from experimental data [4]

2.1.2 Compressibility

As mentioned, compressibility modelling is an indispensable part of simulating real gas behaviour. For this work, the Soave-Redlich-Kwong (SRK) equation was implemented to satisfy this purpose. Although the Bennedict-Webb-Rubin (BWR) equation is recommended for gaseous hydrogen compressibility modelling, the SRK equation provides a wider spectrum of temperature resolution [4] and [18]. This is extremely useful for the application investigated here, since system discharging leads to very low temperatures being met inside the tanks [4]. This choice is also supported by Figure 2.3, where the lack of data for low temperatures in the case of BWR equation is apparent. Of course, there is a slight trade-off by resolving the compressibility equation for very low temperatures, which means that the deviation from experimental data grows larger with lower temperatures. The maximum RMS deviation occurred is 1.1% for the SRK equation at a temperature of around 110K. The set of equations that govern the solution of SRK is presented below [4]:

$$
\begin{aligned}
A^* &= 0.4278\alpha \frac{P/P_c}{(T/T_c)^2} \\
B^* &= 0.0867 \frac{P/P_c}{T/T_c} \\
\alpha^{0.5} &= 1 + m\left(1 - T_r^{0.5}\right), \text{ where } T_r = \frac{T}{T_c} \\
m &= 0.480 + 1.574\omega - 0.176\omega^2 \\
\omega &= -0.216 \text{ for hydrogen} \\
\text{thus, } m &= 0.131805 \\
\text{so the compressibility factor} & \\
\boxed{z^3 - z^2 + z\left(A^* - B^* - B^{*2}\right) - A^*B^* = 0} &
\end{aligned}
\tag{2.5}
$$

2.2 Storage vessels

2.2.1 Technical characteristics & Limitations

As mentioned, type IV tanks are capable of withstanding pressure levels upwards of 700 bar, with 700 being the target gas storage pressure. This storage pressure level brings the density of gaseous hydrogen to approximately 40 kg/m^3 under typical ambient temperature conditions, as it is depicted in Figure 2.4 [5]. The relation between pressure and density is not linear, especially at high pressures. Density rises at a lower rate than pressure does, thus, in order to increase the carrying capacity, pressure needs to increase even more than mass does. This means that storage efficiency reduces as pressure increases and, as the storage requirements rise, so does the energy required to satisfy them. The statement above is explained by Figure 2.4. Although storing gaseous hydrogen may appear as an attractive choice, technological limits connected with this technology might be resolved, cost of production remains high [19].

The current state-of-the-art regarding hydrogen storage tanks with the capacity to withhold such high pressures is type IV tanks. Figure 2.5 illustrates one such tank and the main components it consists of. There is an inner layer consisting of dense polymer or aluminum, which is called liner. This layer is thin compared to the outer CFRP layer. This inner layer also prevents hydrogen from permeating through its surface which in turn means that mass losses and temperature drop are limited by its presence. The outer layer is much thicker and slightly more conductive and it mostly serves the purpose of providing structural integrity to the system [20].

The structural characteristics of the tanks become very significant since hydrogen is stored in such high pressure levels. Safety is very important and constitutes a major consideration when designing tanks. As indicated, mechanical energy release under vessel rupture conditions can result in potentially dangerous events. The work performed in [7], indicates that temperature is the leading factor in terms of mechanical energy release. The correlation mentioned is depicted in Figure 2.6 where it is apparent that the argument regarding the importance of gas storage temper-

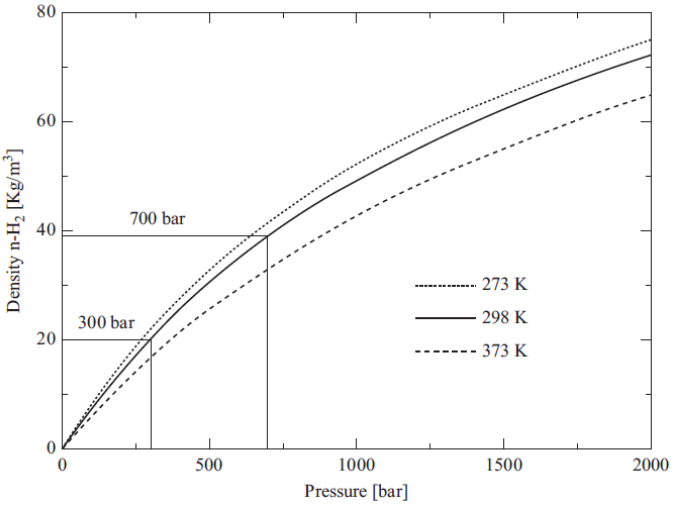

Figure 2.4: Evolution of H_2 storage density as a function of pressure, for various temperatures [5]

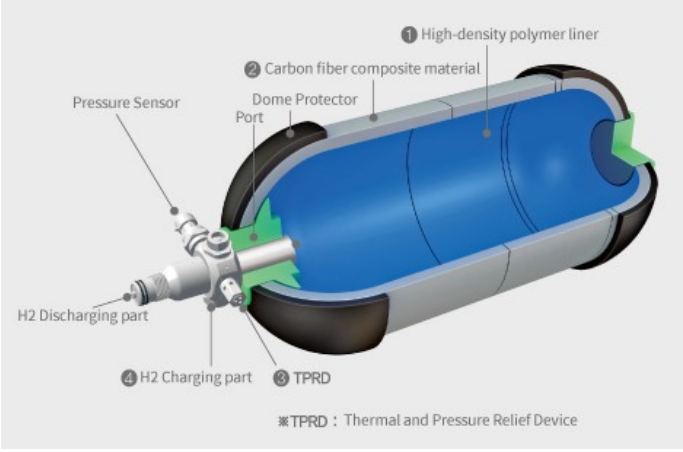

Figure 2.5: Type IV tank cut-section [6]

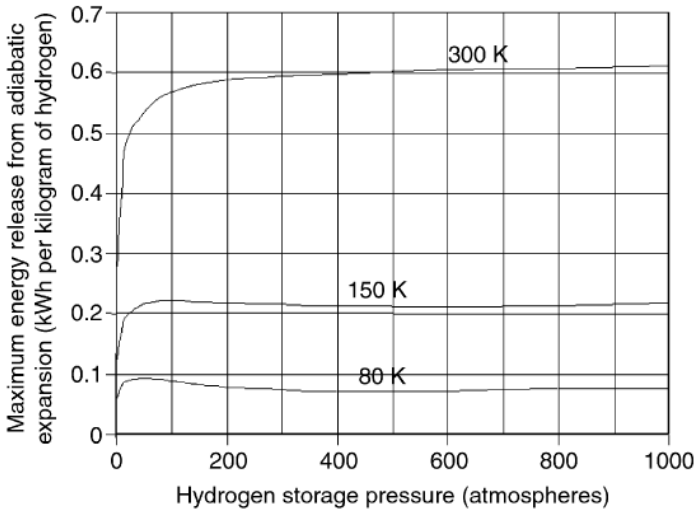

Figure 2.6: Mechanical energy release from pressurized vessels in a rupture event [7]

ature is supported strongly. Figure 2.6 depicts the energy release during the event of rupture in hydrogen carrying vessels, as a function of pressure and temperature. Assuming hydrogen stored in an enclosed vessel at 700 bar, the maximum energy release, should a rupture take place, is almost 3 times higher for 300K gas temperature as opposed to 150K.

2.2.2 Heat transfer mechanism

As indicated by (2.1), heat transfer participation in the temperature profile is important. During isothermal discharge, for example, selecting a very high heat transfer coefficient counters the effects of the $\dot{m}zRT$ term and temperature is maintained constant. Figure 2.7 indicates the different wall layers that construct the tank, as well as the different heat transfer mechanisms that take place during tank emptying. The governing heat transfer mechanisms are convection, between the gas and the inner tank wall as well as the outer wall and the ambient air, and conduction, between the inner and outer wall of the tank. The convective heat transfer is depicted in the right part of Figure 2.7 and the principle by which the heat transfer is described is given by (2.6). In (2.6), Q_i stands for the convective heat transfer between the inner layer and the compressed gas and Q_o stands for the convective heat transfer between the outer layer and the ambient air [8]. In (2.6), h_i and h_o represent the convective heat transfer coefficient for the inner and outer layer of the tank, respectively. A_i and A_o represent the surface area and T_{amb}, T_g, T_{wi} and T_{wo} represent ambient temperature, compressed gas temperature, inner wall temperature and outer wall temperature, respectively [8].

$$\begin{aligned} \dot{Q}_i &= h_i A_i \left(T_{wi} - T_g\right) \\ \dot{Q}_o &= h_o A_o \left(T_{amb} - T_{wo}\right) \end{aligned} \tag{2.6}$$

In (2.6), the term of convective heat transfer coefficient for the inner layer of the

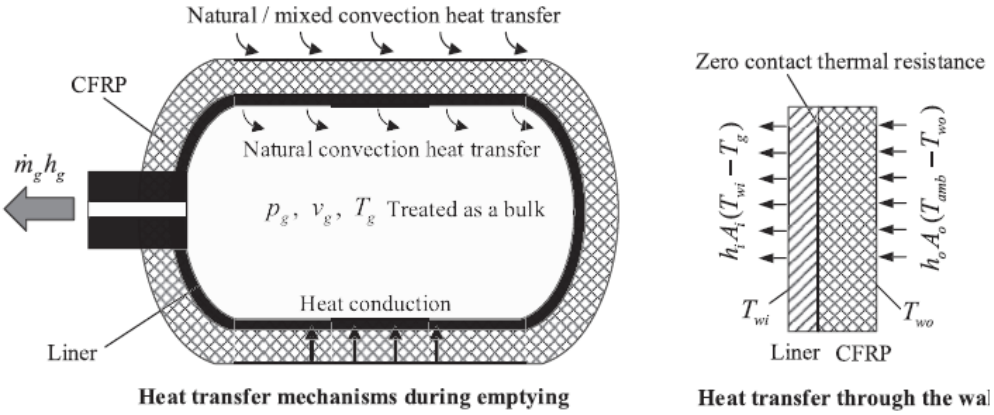

Figure 2.7: Heat transfer mechanism during tank discharge [8]

vessel is calculated by (2.7).

$$h_i = \frac{Nu_i k}{L} \tag{2.7}$$

In (2.7), h_i is the convective heat transfer coefficient with units $[\frac{W}{m^2 K}]$, k is the thermal conductivity with units $[\frac{W}{mK}]$ and L is the characteristic length with units [m], which, in the case of a cylindrical vessel for the purpose investigated here, is its internal diameter. This choice is supported by the fact that the length and the internal circumference of the tank are significantly larger than the wall thickness, thus temperature gradient and, therefore, heat conduction is assumed to occur only along the radial direction [8] and [21].

$$Nu_i = \begin{cases} 1.15 Ra_i^{0.22}, & Ra_i < 10^8 \\ 0.14 Ra_i^{0.333}, & Ra_i >= 10^8 \end{cases} \tag{2.8}$$

The calculation of the Nusselt number for the inner tank wall is provided in (2.8), where the Rayleigh number is given by (2.11), where υ is the kinematic viscosity with units $[\frac{m^2}{s}]$, α is the thermal diffusivity with units $[\frac{m^2}{s}]$, g is the gravitational acceleration with units $[\frac{m}{s}]$, D is the cylinder diameter with units [m], β is the thermal expansion coefficient with units $[\frac{1}{K}]$, T_s is the surface temperature with units [K] and T_∞ is the ambient air temperature with units [K] [22] [23]. The thermal diffusivity value is connected to the materials being used, thus it is a property of the liner and the CFRP layer. Regarding the thermal expansion coefficient β, two methods were investigated for its calculation. The first method was suggested in a study regarding an onboard application of a hydrogen tank with the expression as presented in (2.9) [24]. The other method of calculation is presented in (2.10) and it includes the gas pressure and a constant coefficient α_{const} equal to $1.9155 \cdot 10^{-5}$, with units [K/Pa] [23]. A comparison between the two calculation methods was performed in the Simulink hydrogen storage system (HSS) model and it was concluded that, although the coefficient is slightly different for the two calculation methods, as shown in Figure 2.8, the calculation of important scalars such as pressure does not indicate deviation between the two methods used, as illustrated in Figure 2.9. The reason behind this is that the order of magnitude of the thermal expansion coefficient is

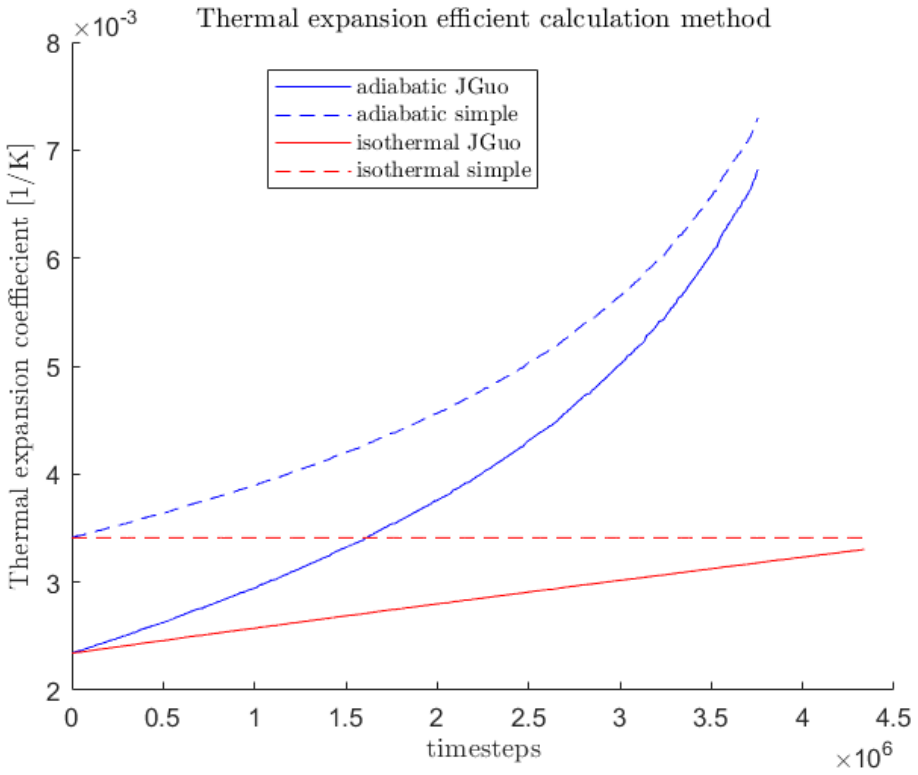

Figure 2.8: Evolution of the thermal expansion coefficient during driving for adiabatic and isothermal cases

relatively insignificant compared to the other participating terms in the Rayleigh number calculation. By examining Figure 2.8, it is clear that the isothermal process produces non-constant β because it is a function of pressure and temperature.

$$\beta = \frac{1}{T} \tag{2.9}$$

$$\beta = \frac{1}{T + \alpha_{const} P} \tag{2.10}$$

The kinematic viscosity calculation is given by (2.12), where μ is the dynamic viscosity and ρ is the gas density. The units of the gas density ρ are [kg/m^3] and the units of dynamic viscosity are [Pa $\cdot$ s]. The dynamic viscosity is calculated by (2.13), where T is the temperature in [K] for which the calculation is performed, C is Sutherland's constant for hydrogen, μ_0 is the reference dynamic viscosity of hydrogen for which experimental data are available. Specifically, the data required for the reference dynamic viscosity refer to the reference temperature T_0 [25]. Table 2.1 presents the reference values, relevant to the calculation of dynamic viscosity.

$$Ra_D = \frac{gD^3\beta\,(T_s - T_\infty)}{\upsilon\alpha} \tag{2.11}$$

$$\upsilon = \frac{\mu}{\rho} \tag{2.12}$$

C	72
μ_0	0.00876 centipoise
T_0	528.93 °R

Table 2.1: Values contributing to the calculation of dynamic viscosity

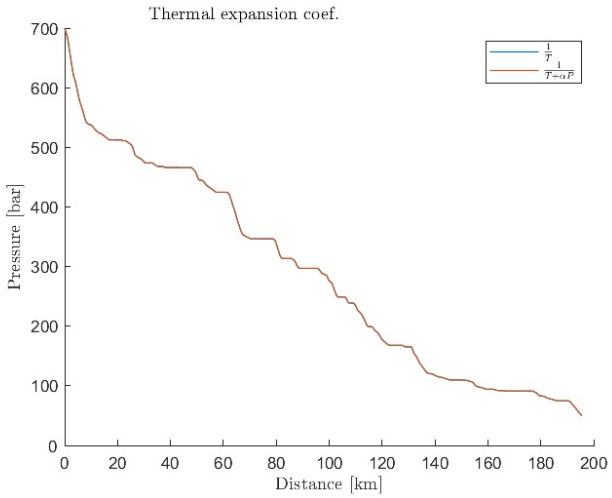

Figure 2.9: Thermal expansion coefficient calculation methods produce identical results

$$\mu = \mu_0 \left(\frac{0.555 T_0 + C}{0.555 T + C} \right) \left(\frac{T}{T_0} \right)^{3/2} \tag{2.13}$$

For the compressed hydrogen case investigated in this thesis, the gas stored inside the tank is treated as bulk. The convective heat transfer inside the tank is dominated by natural convection since the velocities are very low [8]. For the outer wall of the tank, the treatment is slightly different since the convection mechanism is governed by the ambient air temperature and velocity and the assumption holds that these tanks are placed on a moving vehicle that is in direct contact with ambient air. Subsequently, the convective heat transfer mechanism for the outer tank wall might be natural or mixed, depending on the ambient air properties, which would in turn depend on the vehicle and the HSS design within it [8], [22] and [26].

2.2.3 Initial gas temperature effect

During tank discharge simulations, tanks are assumed to be exposed to ambient air conditions. Since it is very important to maintain hydrogen temperature in a reasonable range, it makes sense to investigate the ambient temperature effect on the discharge process. In order to examine that, a simple test was performed as illustrated in Figure 2.10, where the ambient temperature was configured to match the initial tank temperature, so the stored gas-ambient air system was initially considered to be in equilibrium. For the adiabatic discharge process illustrated in this figure, ambient temperature seems to play an important role, since at the

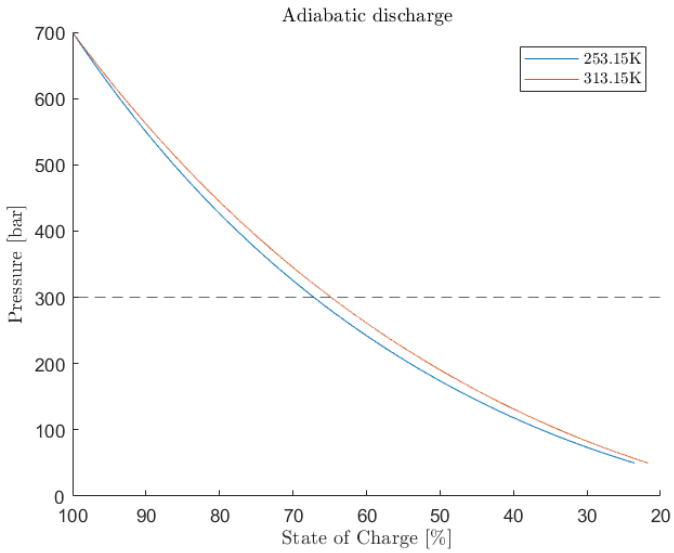

Figure 2.10: Pressure as a function of state of charge for two different ambient temperatures

time-point when the 313.15K case reaches 300 bar, in the 253.15K case the tanks have discharged almost 3% more. It is possible that such temperatures might be encountered in real driving conditions. For the typical ambient temperature range encountered, the difference in remaining pressure would be even less significant. Figure 2.10 illustrates that it is preferred to initiate with the highest possible ambient temperature and make use of the maximum amount of fuel possible before the target pressure of 300 bar is reached inside the tanks. Since heat transfer is not modeled here, it is not the ambient temperature itself that gives the difference in the results, but the starting temperature of H_2 inside the tanks. By that assumption, for the higher temperature case, the c_v would also be higher, hence the temperature drop would be lower, which is also supported by (2.1), and hence the pressure drop would also be lower.

3
Methods

3.1 Model development

The scope of this thesis consists of analysing and defining the properties of a multi-component system, mainly from a thermodynamical point of view. An initial proposed configuration for such a system consists of the storage vessels or tanks, which are the Type IV storage tanks introduced in the previous chapter, the gas booster, whose purpose is to compress the stored gas in order for it to meet the injection pressure and flow rate demand of the engine, some auxiliary equipment such as a cooler, valves, throttle or an expander which would be located downstream of the gas booster, and the system piping, delivering the fuel between components. A sketch describing the above system is provided in Figure 3.1. Gas boosting is necessary in this application, because, as mentioned, the assumed injection pressure is around 300 bar. Since the initial gas pressure in completely filled storage vessels is 700 bar, a certain amount of fuel can be utilized before the tanks can no longer be able to meet the injection pressure demand of the engine. This is the point where the operation of the compressor is essential to the system, otherwise there would be no engine power production to meet the load. Global simulation platform (GSP) is a Volvo developed Simulink model that is configurable with the various parameters required to simulate driving conditions, range, engine, vehicle and various other quantities. The development stages of this model can be discerned in two main parts: the standalone model and the GSP-integrated model. Both of these models are 0D simulation models since there is no spatial dimension involved in the differential equations that govern the thermodynamics of the system. There exist only the temporal dimension and the thermodynamical properties. Chronologically, the standalone model was developed first on MATLAB's platform Simulink. The main components of this model were then developed further and constructed in a manner that an integration with GSP would be feasible. GSP is a proprietary simulation platform developed by Volvo Trucks in Simulink and it is connected with various company projects as a tool to analyze and contribute to decisions regarding existing and future concepts. It can simulate various drive-cycles that trucks perform, so this platform incorporates real world conditions and constitutes a realistic model.

Upon establishing the connection between GSP and the developed model, the simulation results were validated against GT-Power results. Once the validity of the model had been established and the HSS model proved to produce almost identical results as the GT model does, it was necessary to develop a method to produce results closely connected with the purpose of this thesis. A fitting name for the

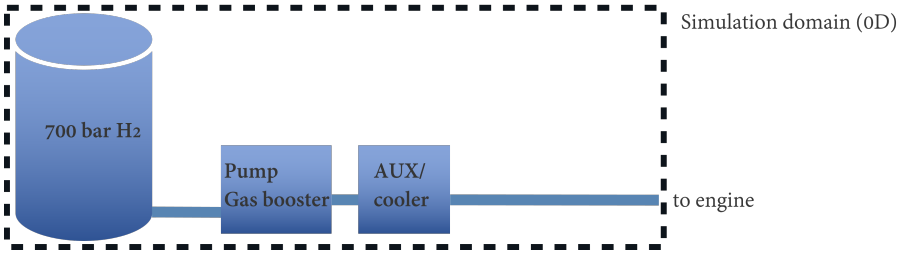

Figure 3.1: Simplistic depiction of the simulation domain

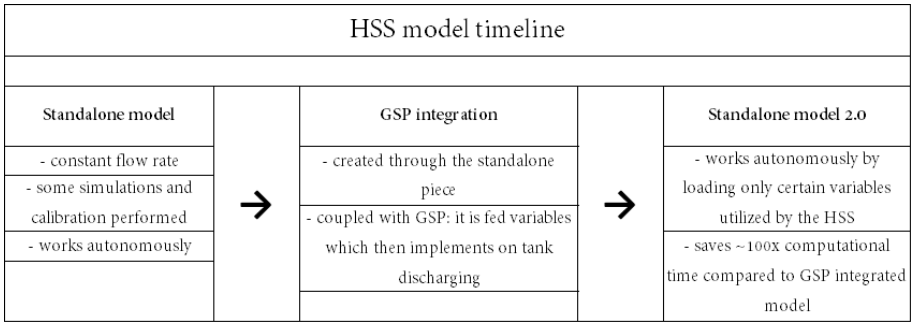

Figure 3.2: Model development timeline & stages of construction

system of blocks developed as part of the work of this thesis would be hydrogen storage system (HSS) and will be mentioned as such from this point on. Since GSP includes a great number of parameters for the different drive-cycles, such as wind-speed, instantaneous power consumed by the various engine components and others, it would not make sense to continue solving these quantities on every time-step. For this purpose, the variables directly connected with the HSS were retrieved by GSP and saved under the corresponding drive-cycle. Namely, these variables are: brake torque, engine speed, vehicle speed and engine flow rate. The model timeline, as well as the different stages of construction, is depicted in Figure 3.2.

From now on, the default simulation platform reported will be the most updated version which is the second version of the standalone model, unless specified otherwise.

Concerning the GSP-integrated state of the HSS involves passive functionality, which means that, while the simulation is running, variables are being used by the HSS, performing the tanks discharge operation and solving the thermodynamical properties involved in the process. The HSS block currently uses parameters from the main GSP, as depicted in Figure 3.6. These parameters are engine speed, fuel consumption, brake torque and gas rail pressure. The fuel flow is initially provided in terms of milligrams per stroke and through the procedure depicted in Figure 3.5 it is conversed into appropriate units of kg/sec. In Figure 3.5, there are two conversion procedures taking place. Firstly, the fuel consumption is provided in terms of mg/stroke and it is converted into kg/sec through a procedure depicted in Figure 3.5. After this conversion, a multiplication with $10^{-}6$ is necessary to convert mg/sec to kg/sec. As far as the second conversion is concerned, it regards energy content conversion in order to account for hydrogen instead of diesel which was previously the case. For this type of conversion, it is adequate to multiply the fuel flow with

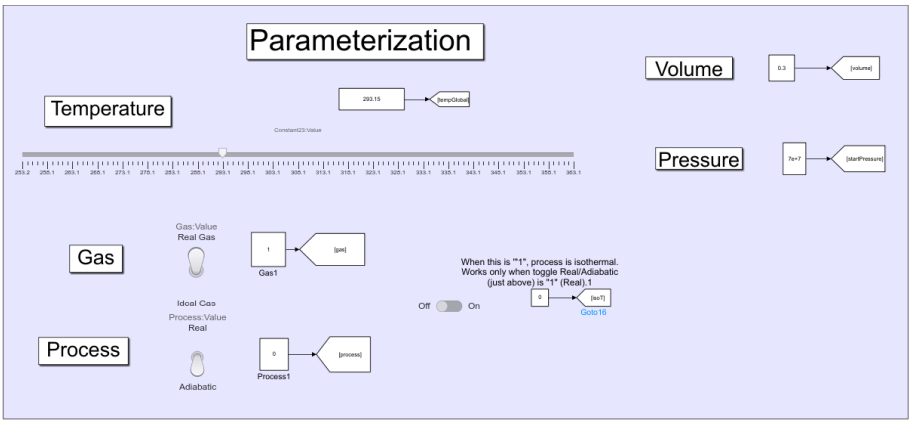

Figure 3.3: Simulink initialization blocks

the ratio of diesel LHV over hydrogen LHV. Since this ratio is approximately 0.36, this indicates that hydrogen consumption must be around 3 times less than diesel to provide the same chemical energy required by the ICE. The 4 parameters mentioned above, constitute the external information needed to run the simulation. Apart from those, there is a number of internally defined parameters that are necessary and are able to configure different cases for the simulation. Figure 3.3 illustrates a set of the most important of these parameters needed to initialise the simulation. The options configured in this set of blocks will be true for every tank in the system. Some configurable options are connected to the discharge process, which might be isothermal, adiabatic or real and others are related to the gas itself, providing the option to switch between ideal and real gas. The ideal gas option was used in the first stages of the model development in order to perform initial model validation. The user can also initialize volume and pressure of the vessels, as well as initial temperature. It is important to mention that temperature is considered global for the system. This assumption supposes that the system has been exposed to the environmental conditions where discharge takes place, for a sufficient amount of time. As such, the temperature of the vessel wall and the gas itself are in equilibrium with the ambient temperature.

As stated above, compression is necessary at some point during tank discharging, as the pressure in the tanks reduces from 700 bar down to 300 bar and below. A suitable compressor for this purpose would be a reciprocating compressor, single or double acting. The reason behind the choice of the compressor being reciprocating is hydrogen's low molar weight [5] and [12]. Another important characteristic of such boosters is the fact that they are sealed properly in a manner that would not allow for the hydrogen molecules to escape the compression system due to their small size. Figure 3.4 illustrates the compression energy required to increase hydrogen pressure, as percentage of the HHV of hydrogen in MJ/kg [9] and [27]. As shown, the two extremes among which the real compression will operate, are the adiabatic and isothermal compression processes. In the adiabatic compression, no heat exchange takes place between the hydrogen and the ambient and it essentially takes place under constant entropy [27]. Under the assumption of the isothermal process, on the other hand, the gas temperature remains constant throughout the compression

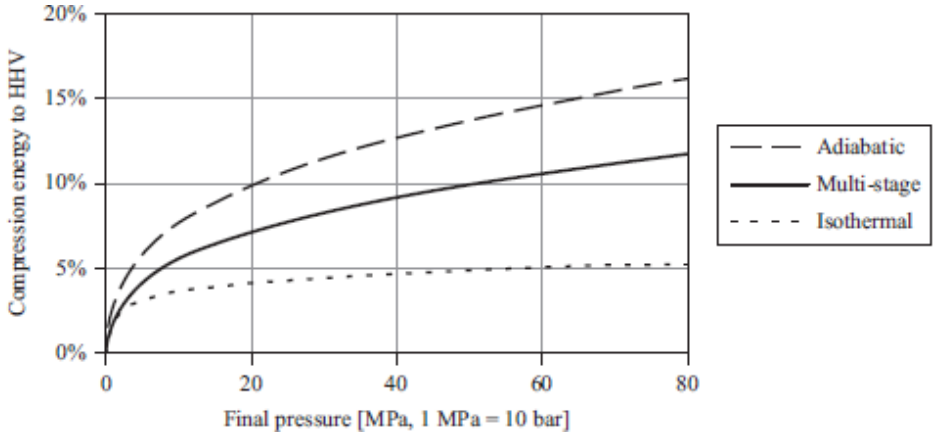

Figure 3.4: Compression energy required as a function of final pressure [9]

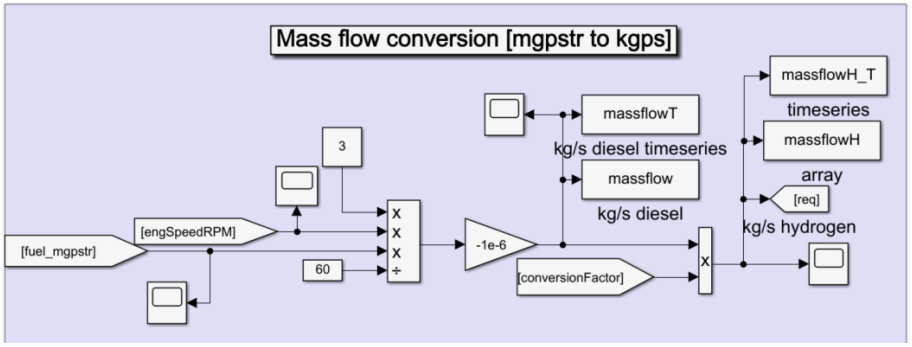

Figure 3.5: Fuel flow conversion technique

process. For increased system efficiency, the real compression process line should lie as close to the isothermal as possible. Another important point extracted by examining Figure 3.4, is that the lower the gas pressure is, the more costly it is to bring it to useful levels of pressure, which would be around 300 bar as previously stated. The cost is 4.5% to raise the gas pressure from 50 to 300 bar, while it is 3.5% to raise the gas pressure from 300 to 800 bar. The percentage refers to the ratio of compression energy over hydrogen HHV. Since the first case of compressing from lower pressure levels fits the application assumed in this work, approaching the isothermal compression process would significantly reduce the compressor operation cost.

The purpose of this work does not involve investigating injection strategies and how these will affect the system, as a whole. Nevertheless, some background information is needed in order to understand the general context and specific choices that were made. The choice for the assumed injection pressure of 300 bar is based on the assumption that the H2 combustion system would behave similarly to the one using natural gas. Engine tests and simulations have shown that this assumption is generally true, thus 300 bar injection pressure is a good starting point for the HPDI H2 engine development. Hydrogen has a very high auto-ignition temperature of around 853K, while for diesel, for example, the auto-ignition temperature is around 523K. This work mainly assumes that hydrogen is directly injected in the cylinder at a late compression stage, with diesel pilot injection. Diesel pilot is only used to ignite H2

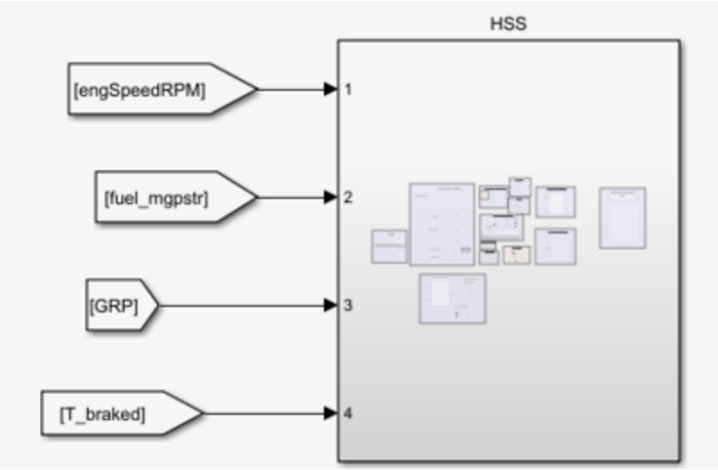

Figure 3.6: The HSS block incorporated in GSP

a_1	2.3443112
a_2	7.98052075 $\cdot 10^{-3}$
a_3	-1.9478151 $\cdot 10^{-5}$
a_4	2.01572094 $\cdot 10^{-8}$
a_5	-7.37611761 $\cdot 10^{-12}$

Table 3.1: Coefficient values for hydrogen c_v - NASA polynomials, temperature range 200 - 1000K

as the latter has too high auto-ignition temperature [28], [29] and [30].

As shown in (2.2), the temperature profile is given by a differential equation containing temperature itself. For this purpose, the Simulink model constructed to illustrate the equation consists of a loop, containing an integrator that provides an initial condition to the system, as depicted in Figure 3.7. The specific heat under constant volume c_v calculation was performed through NASA polynomials coefficients for hydrogen through (3.1). The coefficients used are provided in Table 3.1. This analytical calculation of the specific heat decreases the error in the calculation performed, although there is no significant deviation with the results calculated with constant c_v of 10160 J/kgK.

$$c_v = \left(a_1 + a_2 T + a_3 T^2 + a_4 T^3 + a_5 T^4\right) R - R \tag{3.1}$$

The set of blocks illustrated in Figure 3.8 was employed in order to simulate the instantaneous hydrogen mass in the tanks. The advantage of this system is that it can be copied and used for each tank, independent of the total number of tanks in the system. It uses the mass flow requirement adapted to hydrogen, as described in Figure 3.5 as well as the initial hydrogen mass for each tank participating in the system. With the input described above, it calculates the instant hydrogen mass through an integrator block and it feeds it as input in order to calculate the thermodynamical properties of the specified tank.

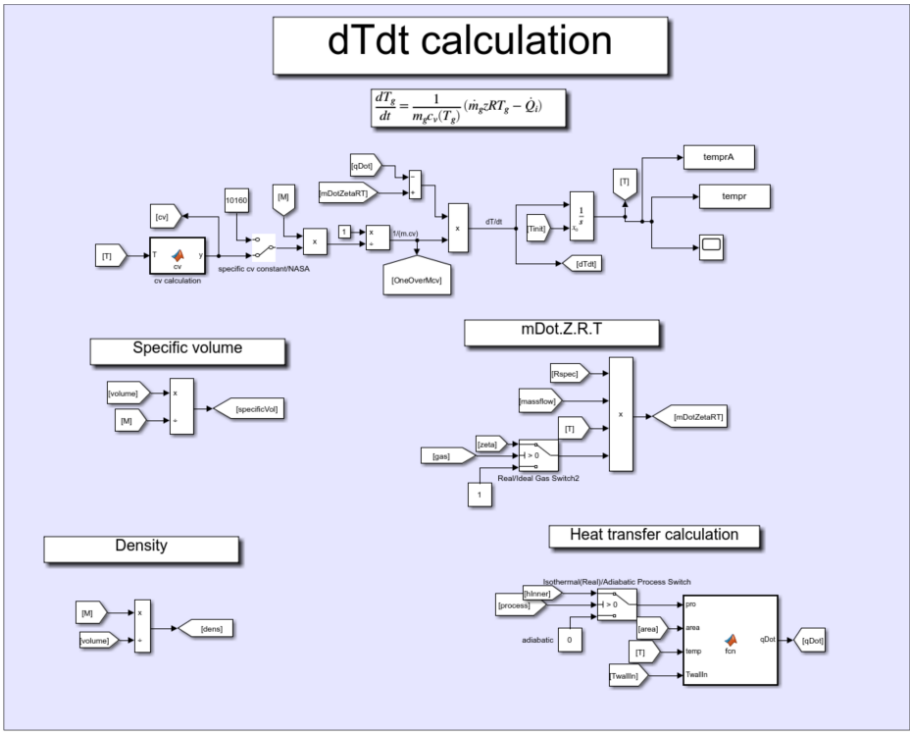

Figure 3.7: The temperature profile calculation blocks

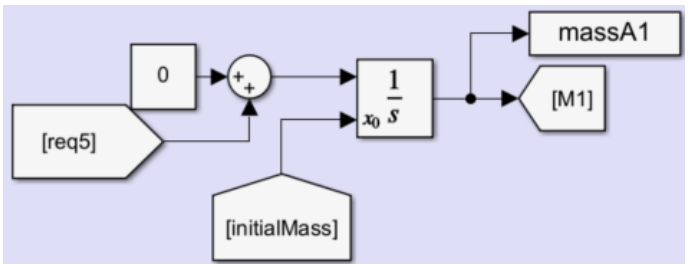

Figure 3.8: Mass integration blocks - HSS

3.2 Standalone model 2.0

As stated, the need to save valuable computational time led to the development of the final and most updated version of the standalone model, which incorporates the model's capability to simulate a number of different drive-cycle scenarios, without the need to unnecessarily solve all the drive-cycle quantities that are not affected by change in the HSS setup.
Standalone model 2.0 is able to solve the typical drive-cycles in the order of minutes and is found to be almost 100 times faster compared to running the entire GSP model. The inputs used in this version are presented in Figure 3.9 and they were retrieved from company files containing the relevant information for the corresponding drive-cycle. It has been mentioned before, but it is useful to repeat that these quantities are torque, total flow rate to the engine, which contains the LHV mass conversion, engine speed and vehicle speed. All of these quantities are provided in S.I. units, with engine speed in radians per second. The vehicle speed was provided in order to calculate the distance achieved in each drive-cycle via signal integration. For each of these variables that are externally loaded in the Simulink model from .mat files created in MATLAB workspace, the loading sample rate was selected so as to match the sample rate at which they were retrieved from GSP.
The improvements that this version of the model underwent compared to the GSP-integrated version are described below. First of all, the interface had to be re-designed, since a major component was accounted for in the model. This component is the buffer tank which will be analyzed further in the respective section. In order to briefly justify the buffer existence, it is sufficient to say that it is responsible for matching the engine flow rate and pressure demand, by alleviating the need for a large compressor.
Another model segment that underwent changes is the tank model itself. Although the initial model development stage, namely the first standalone model and the GSP-integrated version, consisted of several blocks to execute simple tasks such as adding or multiplying signals, in standalone 2.0 most of these tasks were compiled in a single function for each tank, consisting of multiple inlet/outlet signal ports, as depicted in Figure 3.10.

3.3 Heat transfer modelling

3.3.1 General notes

In order to simulate heat transfer between the stored gaseous hydrogen, the storage vessel and the ambient air, (2.6) was employed in a global form, as illustrated in (3.2). The heat transfer coefficient h, is estimated through the Nusselt and Rayleigh number as illustrated in (2.7) and (2.11). The current state of the model contains all the relevant blocks to perform these calculations but they are inactive. This choice was made to perform simplified calculations as an initial indication. Upon retrieving some data, those blocks shall be activated and complexity will gradually be introduced in the HSS. The current state of the simulations consists of two extremes selected in order to provide the whole operation spectrum of the heat transfer

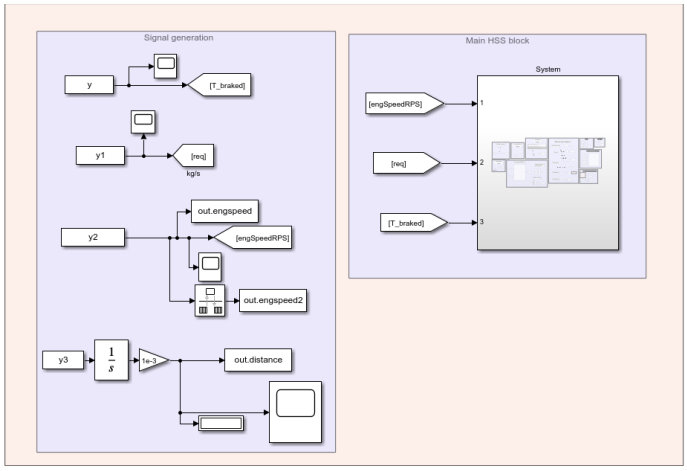

Figure 3.9: Main quantities retrieved from Volvo Group drive-cycles

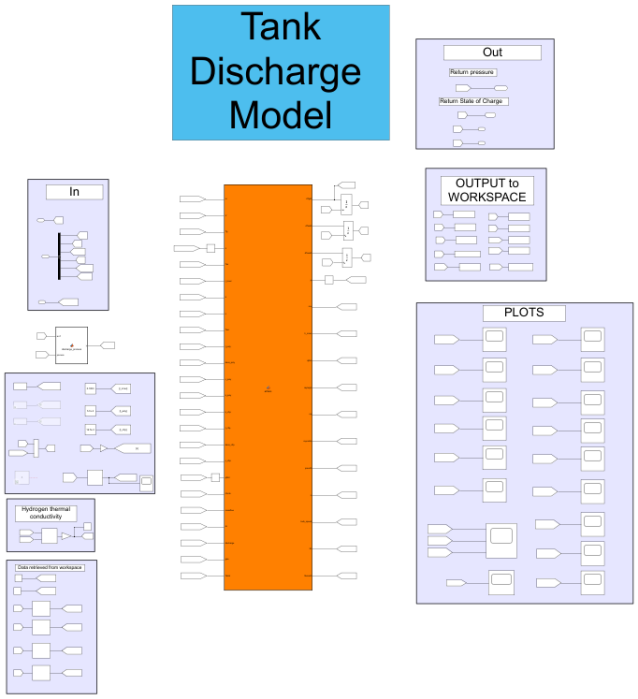

Figure 3.10: Updated tank model with a single function solving thermodynamical quantities

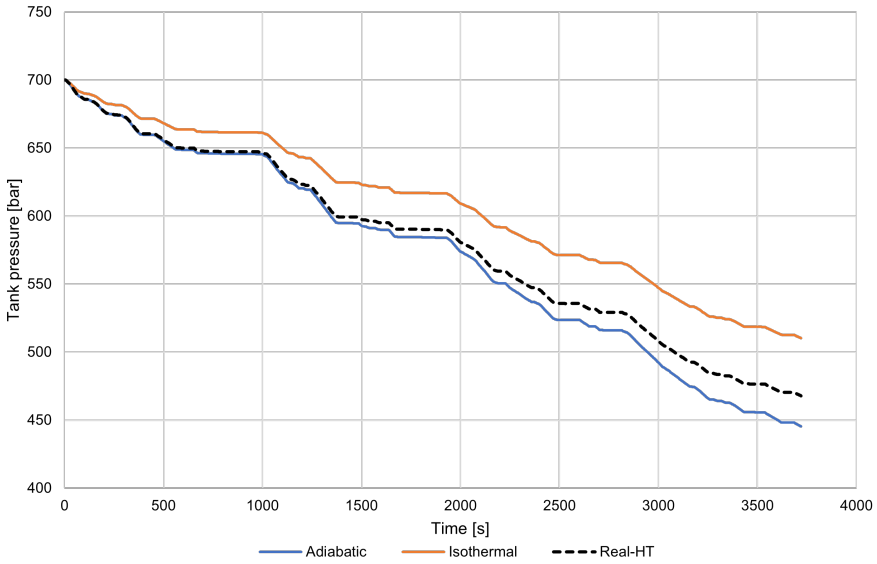

Figure 3.11: GT-Suite simulation of tank pressure as a function of time, implementing different heat transfer models

model. This operation spectrum will lie between two processes, the adiabatic and the isothermal process, similar to the compressor operation.

$$\dot{Q} = hA\,(T_w - T_g) \tag{3.2}$$

In order to extract some initial results regarding the real vessel discharge process and to validate the developed Simulink model, a simplified tank model was developed in GT-Suite, employing real gas equations and type IV tank technical properties. The results of these simulations are presented in Figure 3.11. The simplified GT model constructed is shown in Figure 3.12. With more realistic wall heat transfer estimations, the gas pressure during the discharge process tends to fall between the adiabatic and isothermal results, as expected. However, initially when the temperature drop is not large, the real heat transfer case tends to follow the adiabatic curve, whereas later in the drive-cycle when the temperature drop is larger, the heat transfer increases and the process moves closer to the isothermal discharge. Generally, this exercise shows that, as an initial simplification, the real discharge process can be assumed to be an average between the isothermal and adiabatic processes. However, it also demonstrates the need to develop accurate heat transfer models, which is further presented in Section 3.3.2. Regarding the simulated adiabatic and isothermal processes, they were applied in the heat transfer by substituting h in (3.2) with the value of 0 $W/(m^2K)$ for the adiabatic and 10^5 $W/(m^2K)$ for the isothermal case.

3.3.2 Application-specific modelling

As illustrated in Figure 3.11, the real discharge process is much closer to the adiabatic emptying process than to the isothermal one in the beginning of the process,

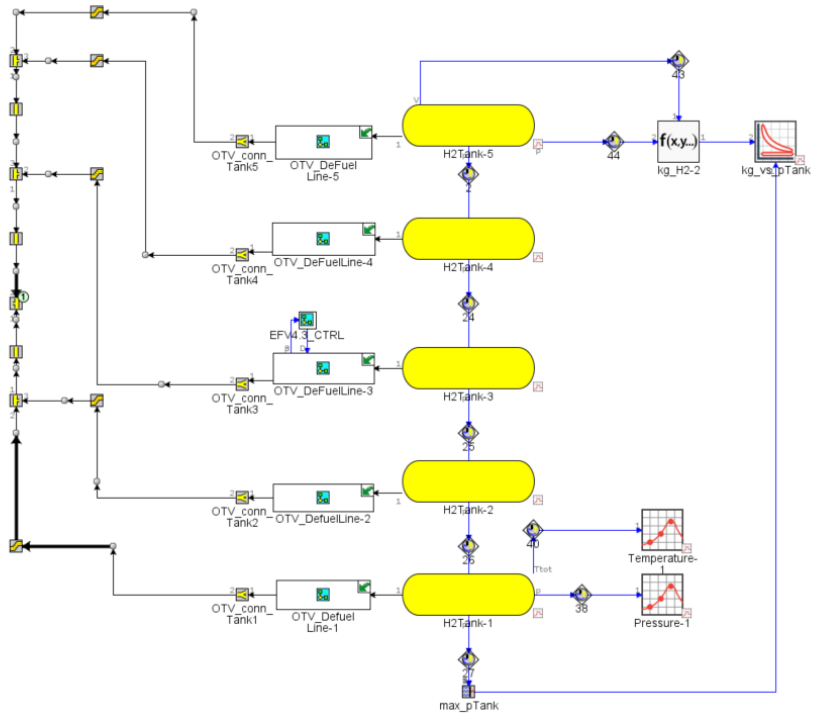

Figure 3.12: GT-Suite domain, *property of Volvo Group AB*

while the situation is reversed towards the end of the emptying process. It is also clear that the isothermal discharge process is the most advantageous, since for the same discharge time it is responsible for a higher remaining pressure inside the storage vessel. In Figure 3.13, a quantification of this difference in tank utilization is provided. In this illustration, a constant mass discharge rate was employed for the two processes. A 12% difference is noted in terms of state of charge in the tanks, upon comparing the two extreme cases for the two corresponding emptying processes. With the isothermal process, the tanks reach the target pressure of 300 bar having used around 47% of the stored hydrogen mass. The corresponding tanks utilization with the adiabatic process reaches approximately 34.5%. With the isothermal discharge process, more hydrogen mass is consumed before the target pressure is reached, thus making this type of process more advantageous from the compression energy preservation standpoint, where the compressor can be used less which leads to improvement of the overall system efficiency and fuel consumption. The x-axis of Figure 3.13 represents the tanks state of charge and is calculated as the initial hydrogen mass over the instantaneous mass during discharge.

In order to fully grasp the heat transfer mechanism employed to simulate tank discharging, refer to Figure 3.14. The gas inside the tank was treated as bulk and the inner aluminium layer and the outer CFRP layers were treated as the inner and outer walls, respectively. Between the gas and the inner wall, heat is exchanged through convection. The same is true for the ambient air and the outer wall. In the case of the inner to outer wall, heat is exchanged through conduction and it was assumed that the connecting point of these 2 surfaces has a zero-contact thermal resistance, which means that no air layer exists between the two material surfaces.

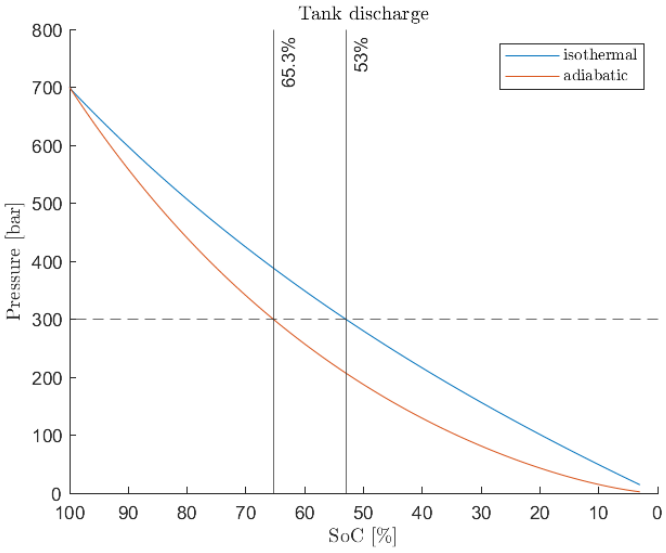

Figure 3.13: Tank pressure as a function of state of charge during isothermal and adiabatic discharge processes

In the simulations performed for the scope of this thesis, ambient air temperature was held constant, which is quite realistic since a truck would not travel for more than 4 or 5 hours at a time and, during that time, the environment temperature would be somewhat steady. In spite of that, it had to be established that the model could handle a varying ambient temperature scheme in its calculations and indeed it was proven that a varying scheme loaded through prerecorded data in the workspace did not pose a problem for the model.
The experimental nature of the tank discharging application requires a different expression for the Nusselt number to simulate heat transfer between the gas and the inner tank wall. The expression in (2.8) might be sufficient for certain applications, but, for this project, it is not considered sufficient since it does not incorporate forced convection. Instead, it only incorporates natural convection with the use of Rayleigh number and, for this reason, (3.3) was employed to simulate the Nusselt number between the gas and the inner tank wall [31]. In (3.3), Ri is the Richardson number and it expresses the ratio of buoyancy term over the flow shear term. In the simulations performed in the progress of this thesis, the Richardson number was almost always found to have values much higher than 0.1, thus convective heat transfer between the gas and the inner tank wall is always mixed: natural and forced. The Richardson number is expressed by (3.4), with the Prandtl number expressed by (3.5) and the Reynolds number given by (3.6). Regarding the Prandtl number, μ represents the dynamic viscosity with units [Pa·s], c_p represents the specific heat capacity with units [J/kg/K] and k is the thermal conductivity with units [W/m/K]. Regarding the Reynolds number, since it is a 0D model, the stored gas is treated as bulk and velocity V is given by (3.7). In the case of Reynolds number calculation, the characteristic length L is the tank diameter.

$$Nu_i = \begin{cases} \mathrm{Nu}_{\mathrm{forced_x}}, & Ri < 0.1 \\ \mathrm{Nu}_{\mathrm{mixed}}, & \text{otherwise} \end{cases} \tag{3.3}$$

$$\mathrm{Ri} = \frac{\mathrm{Rayleigh}}{\mathrm{Prandtl}\ \mathrm{Reynolds}^2} \tag{3.4}$$

$$Pr = \frac{\mu}{c_p k} \tag{3.5}$$

$$Re = \frac{\rho V L}{\mu} \tag{3.6}$$

$$V = \frac{\dot{m}}{\rho r_{inner}^2 \pi} \tag{3.7}$$

Rayleigh number in (3.4) is given by (2.11), provided in the previous chapter. The Nusselt number terms in (3.3) are provided analytically in (3.8) and, as mentioned previously, mixed convection is prevalent during tank discharge [31]. Apart from (3.2) which describes convective heat transfer between the gas and the inner tank wall, it is also required to model conductive heat transfer between the two tank layers, as well as convective heat transfer between the outer tank layer and the environment. Employing the resistance-based heat transfer model, it is possible to write the corresponding differential equations for the calculation of inner and outer tank wall temperatures, in each time-step, given by (3.9) and (3.10), respectively. Subscripts i and o refer to the inner and outer tank wall layers, which correspond to aluminium and carbon fibre, respectively. In (3.9) and (3.10), t, ρ and c represent layer thickness, density and specific heat capacity, respectively. Heat transfer coefficient h for the inner layer is provided in (2.7), while, for the outer layer, this parameter was tested in a range of values rather than estimated by analytical calculation and will be analysed further in the *Results* chapter. T_{amb} is the ambient temperature and is held constant during the simulation and k is the thermal conductivity with units [W/m/K]. All of the above values connected with material properties were retrieved from data circulating within Volvo Group and will be withheld from publishing in this thesis.

$$\begin{aligned} \mathrm{Nu}_{\mathrm{forced_x}} &= 0.7Re^{0.67} \\ \mathrm{Nu}_{\mathrm{natural}} &= 0.104Ra^{0.352} \\ \mathrm{Nu}_{\mathrm{mixed}} &= (\mathrm{Nu}_{\mathrm{forced_x}}{}^{n} + \mathrm{Nu}_{\mathrm{natural}}{}^{n})^{1/n} \\ n &= 4 \end{aligned} \tag{3.8}$$

$$\frac{dT_{w_i}}{dt} = \frac{1}{t_i \rho_i c_i}(h_i(T_g - T_{w_i}) + (\frac{k_i}{t_i/2} + \frac{k_o}{t_o/2})(T_{w_o} - T_{w_i})) \tag{3.9}$$

$$\frac{dT_{w_o}}{dt} = \frac{1}{t_o \rho_o c_o}(h_o(T_{amb} - T_{w_o}) + (\frac{k_i}{t_i/2} + \frac{k_o}{t_o/2})(T_{w_i} - T_{w_o})) \tag{3.10}$$

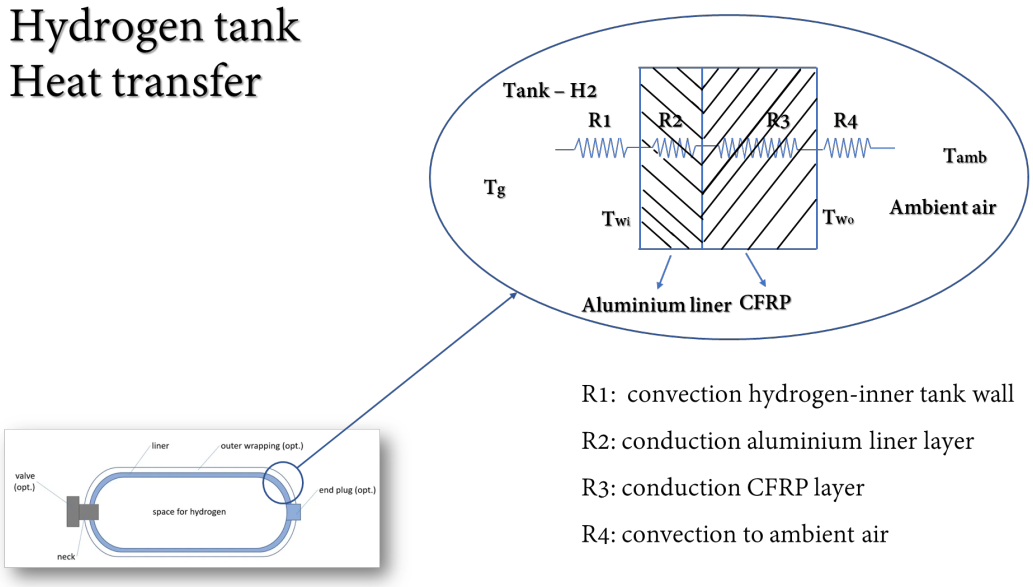

Figure 3.14: Heat exchange between the gas and ambient air takes place via 2 different methods: convection and conduction

3.4 Compressibility modelling

Upon examining the divergence between ideal gas modelling and real gas modelling, it was concluded that the simulations should be performed under the real gas assumption. This choice is also strongly connected with the high storage pressure of hydrogen. As it is illustrated in Figure 3.15, above a given pressure value, the Joule Thomson coefficient becomes negative. This means that, while the coefficient is negative, temperature rises while the pressure drops. Thus, while the gas expands, it is heated instead of cooled during a Joule-Thomson expansion process. This counter-intuitive action takes place for negative values of the Joule-Thomson coefficient and the way this coefficient acts on the gas is summarized in Table 3.2 [10]. In Figure 3.15, 3 different areas can be discerned. The area where μ_{JT} is positive, which is located below the inversion temperature, the area where μ_{JT} is negative, which is located above the inversion temperature, and the line where μ_{JT} is zero, which is the case for ideal gases where the Joule-Thomson effect does not take place. The inversion temperature for hydrogen is low compared to other gases, around 190K [12]. Equation (3.11) can be used to estimate the JT coefficient which is expressed as the rate of change of temperature with respect to pressure, under constant enthalpy. For ideal gases, temperature does not exhibit any variation with pressure, under the isenthalpic assumption. The contribution of the JT coefficient is not taken into account in the model constructed, since it is not considered to have a significant impact and it is intentionally disregarded. The explanation lies on the fact that the JT effect only takes place during the so-called Joule-Thomson expansion, which is an isenthalpic process of passing a higher pressure gas through an orifice and expanding it to a low pressure on the other side of the orifice without any heat transfer. Basically, it means that the JT effect may only occur over the

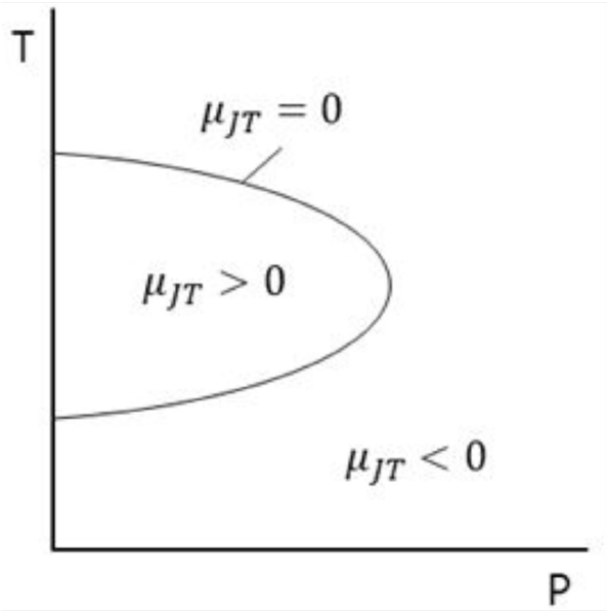

Figure 3.15: Joule-Thomson coefficient

Gas temperature	μ_{JT} **is**	∂P **is**	∂T **must be**	**gas**
below inversion temperature	>0	<0	<0	cools
above inversion temperature	<0	<0	>0	heats

Table 3.2: Joule-Thomson coefficient behaviour [10]

pressure regulator valve, and its effects are known to be quite minor compared to the normal turbulent sonic discharge effects.

$$\mu_{JT} = \left(\frac{\partial T}{\partial P}\right)_H \tag{3.11}$$

For the compressibility coefficient modelling, the set of equations in (2.5) was employed in the HSS. For the purpose of calculating the value of z, which represents compressibility, had to be evaluated on each time-step. The first version consisted of employing an algebraic constraint block in Simulink. As illustrated in Figures 3.16 and 3.17, this tactic consists of constructing a feedback loop. The loop is created due to the fact that compressibility calculation requires pressure, while pressure calculation requires compressibility. This creates an interconnection between the two variables and increases computational time. The algebraic constraint block in Figure 3.16 is internally provided with an initial estimate of compressibility so that it can direct its solution through that. It was concluded that this guided estimation does not play a significant role in terms of saving time or accurately calculating the solution.

Upon compiling the GSP-integrated model, the algebraic loop proved to be problematic for the integrity of the model, especially when trying to run multiple cases in batch mode. The solution arrived by employing numerical methods and, specifically, the Newton-Raphson method. The principle is identical as presented above: the goal is to estimate the compressibility, but this time through an iterative process.

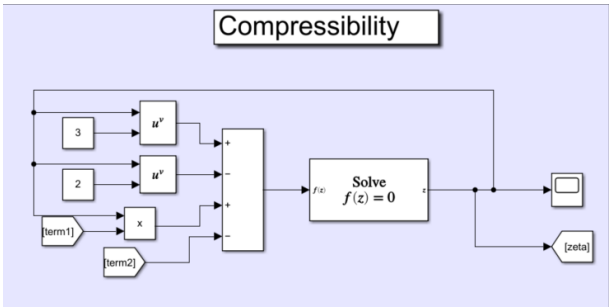

Figure 3.16: Algebraic constraint block solving for compressibility as in (2.5)

For this purpose, as done before, an initial estimate for compressibility was provided and a value for tolerance was set to $10^{-}11$. With the use of a *while* loop inside the main tank function depicted in Figure 3.10, the numerical method was employed in order to obtain the solution. A break was placed inside the loop to avoid countless iterations that would slow down and possibly cause the model to crash. Nevertheless, it was found that convergence was achieved after 2 to 5 iterations, which proves that this method is suitable for the problem at hand. The applied Newton-Raphson method for the compressibility equation in (2.5) is presented in (3.12).

$$\begin{aligned} z_1 &= z_{\text{est}} \\ f(z_1) &= z_1^3 - z_1^2 + z_1(A^* - B^* - B^{*2}) - A^*B^* \\ f'(z_1) &= 3z_1^2 - 2z_1 + (A^* - B^* - B^{*2}) \\ z_{\text{new}} &= z_1 - f(z_1)/f'(z_1) \\ \text{tol} &= \text{abs}(z_1 - z_{\text{new}}) \end{aligned} \tag{3.12}$$

Typical values of compressibility during full tank discharge implemented in a relatively demanding drive-cycle with low gross cargo weight is presented in Figure 3.18. It is illustrated that the compressibility trend is very similar to the one depicted in Figure 2.1.

3.5 Compressor & Buffer modelling

Hydrogen pressure in the storage vessels drops non-linearly with its consumption. It is also illustrated in Figure 3.11 that the real discharge process will lie closer to the adiabatic process, which reaches the target injection pressure of 300 bar faster than the isothermal process does. In a simplified case with just one storage tank, or multiple tanks contributing equally in the engine mass flow demand, the compressor would be required to raise hydrogen pressure up to the requirement of the engine when the hydrogen storage pressure falls below 300 bar, without accounting for system losses. With losses, the compressor would need to begin operating even sooner in order to be able to deliver the required pressure levels to the engine cylinder.
The above system constitutes a simplified configuration of what an HPDI engine might incorporate. In reality, to be able to meet the engine demand for flow rate and pressure in such a direct manner, a very large compressor would be needed. This

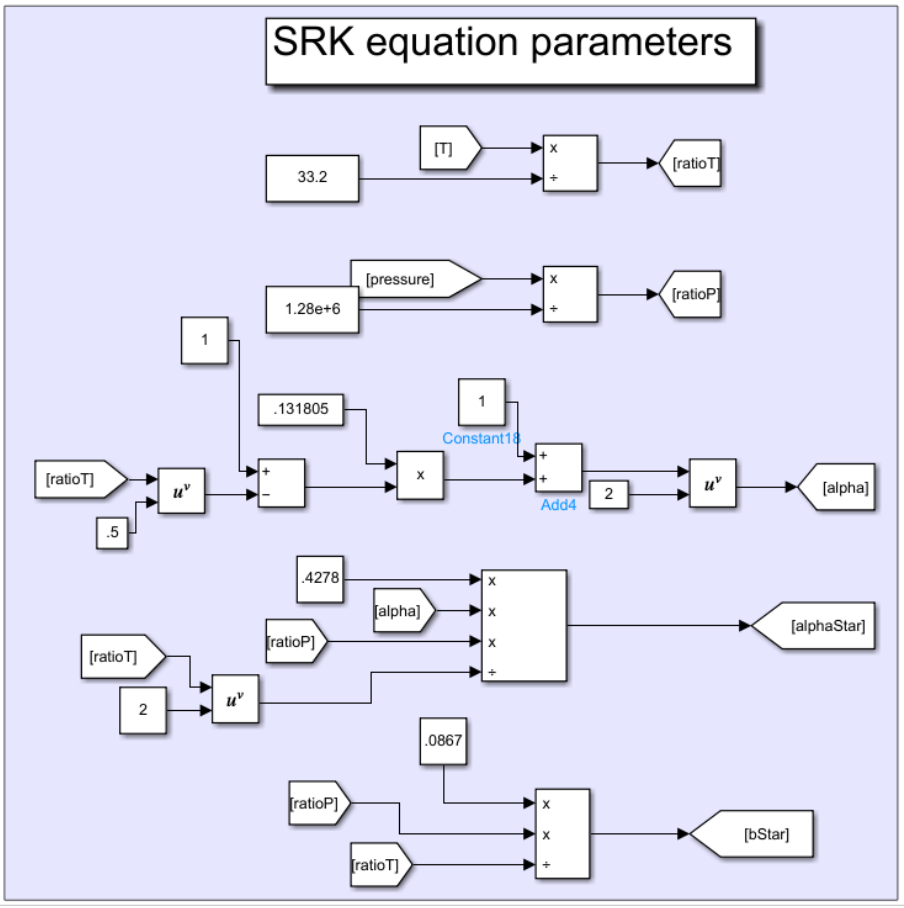

Figure 3.17: Compressibility parameters calculation

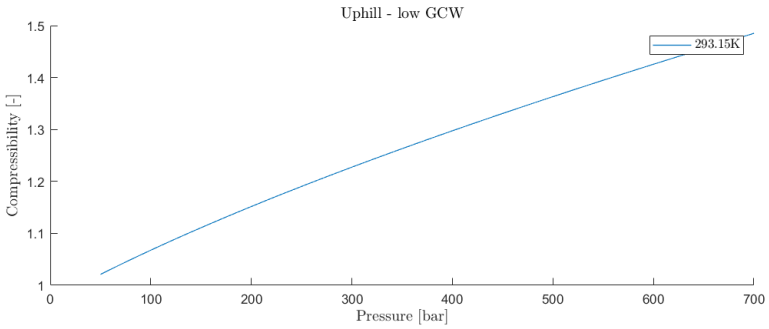

Figure 3.18: Hydrogen compressibility profile during complete tank discharge

would bring manufacturing cost as well as volume cost upwards for such vehicles, thus a more viable solution is considered necessary. The way to counter this issue is to use some type of buffer storage, which is what this thesis incorporated. The integration of the buffer in the system is as follows: the hydrogen gas tanks are connected either with the compressor or with the engine directly. If the connection is established with the engine directly, it means that the tanks are able to meet the engine requirements and no compressor or buffer is needed. On the other hand, if the gas tanks are connected with the compressor, it follows that the buffer will be utilized along with it. That means that the only route from the compressor to the engine is through the buffer. The working principle of the buffer is its discharging and reducing its internal pressure while providing the fuel pressure and flow rate the engine requires, for as long as possible. There exists a user-defined buffer pressure range, during which the tank is used to cover the engine requirements. When the buffer pressure drops below the lower limit of the predefined range, the compressor is activated thus supplying gas to the buffer and raising its pressure. When the buffer pressure exceeds the upper limit of the range, the compressor operation is stopped, thus cutting off the fuel inflow into the buffer and allowing its pressure to start reducing again. The stop function created for the model contains this condition check to avoid endless buffer discharge and, also, to remain realistic in simulating the process. The exact methodology and strategy implemented on the buffer will be defined in a later section of this chapter.

Regarding the compressor modelling, this project was concerned with compressor data available from 2 external suppliers that Volvo Group is in cooperation with, who shall, remain nameless, for intellectual property protection reasons. For the scope of presenting the findings with these two compressors, a naming convention will be established and they will simply be called Compressor 1 and Compressor 2. More information on the findings regarding these 2 compressors will be provided in the Results chapter of this thesis, but for now it is sufficient to briefly comment on the general characteristics of those 2 compressors, to the extent that the IP protection rules allow. Compressor 1 is much smaller in size than Compressor 2 and it is the one that operated in conjunction with the buffer. It was found that the design limits of Compressor 2 were sufficient to cover both flow rate and injection pressure the engine demands, in the drive-cycles data that were tested for the purpose of this thesis. A simple sketch depicting the whole HSS with the interconnections between the different parts simulated is presented in Figure 3.19.

Compressor 1 design was assumed to include only 2 values of injection pressure. To simplify the compressor control, only 2 injection pressures were selected to represent the varying injection pressure in the real engine map. The logic that was implemented to dictate the operation of the compressor is described with the help of Figure 3.20. The intake pressure, which is the pressure at which hydrogen is stored in the vessels, is a decisive factor on the compressor load calculation. The importance of the intake pressure is supported by the fact that, through density, it defines the maximum hydrogen mass flow rate that can be achieved and, thus, dictates whether the engine operation point can be met or not. It should also be noted that the compressor operates only when pressure drops below a certain level and is useful until the vessel pressure reaches 50 bar, which constitutes around 90%

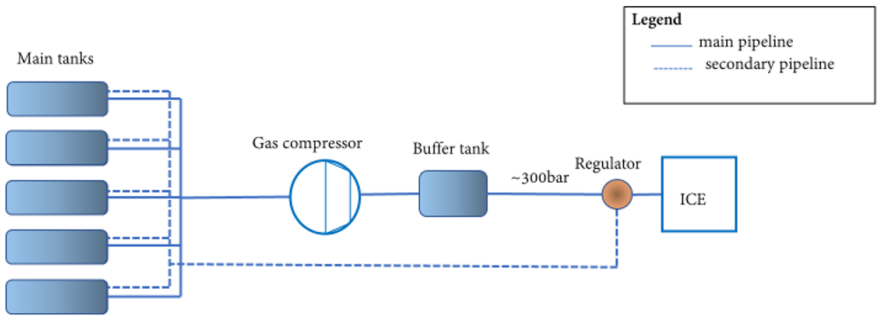

Figure 3.19: Different pipeline routes assumed in order to cover the operating spectrum with Compressor 1

hydrogen mass utilization for the isothermal process and around 78% for the adiabatic process. Mass utilization is defined as the ratio of remaining mass to initial mass of hydrogen stored in the HSS.

3.6 Strategy

In order to put the interconnections and the system described in *Compressor & Buffer modelling* section into perspective, Figure 3.19 will be used. In this thesis, the tank configuration examined was that of a bank consisting of 5 tanks, equally contributing to the engine requirements in terms of flow rate. Both pipeline routes correspond either to Compressor 1 or Compressor 2, depending on usage stage.
There are 4 different strategies implemented in this thesis and these are: simple tank discharging (sd), discharging with the use of Compressor 1, discharging with the use of Compressor 2 and "smart" tank discharging.
Simple discharge is the most simple solution one can come up with upon dealing with the issue of achieving maximum utilisation of fuel in HPDI engines and it involves discharging the tanks until they reach 350 bar pressure which signifies the end of the simulation. It is expected that this strategy will not lead to competitive results, but it serves as a reference for the rest of the simulations, where the compressor will be introduced in the system.
Compressor 1 is the least capable of the 2, as mentioned. Incorporating this compressor in the system is accompanied by inability to either match the injection pressure or the engine flow rate, in certain route points and tank pressure levels. For this reason, the buffer recharging technique was simulated, as described in Section 3.6. This recharging technique is simulated in parallel with the tank discharging in the form of a function in Simulink model and it consists of a simple set of rules:

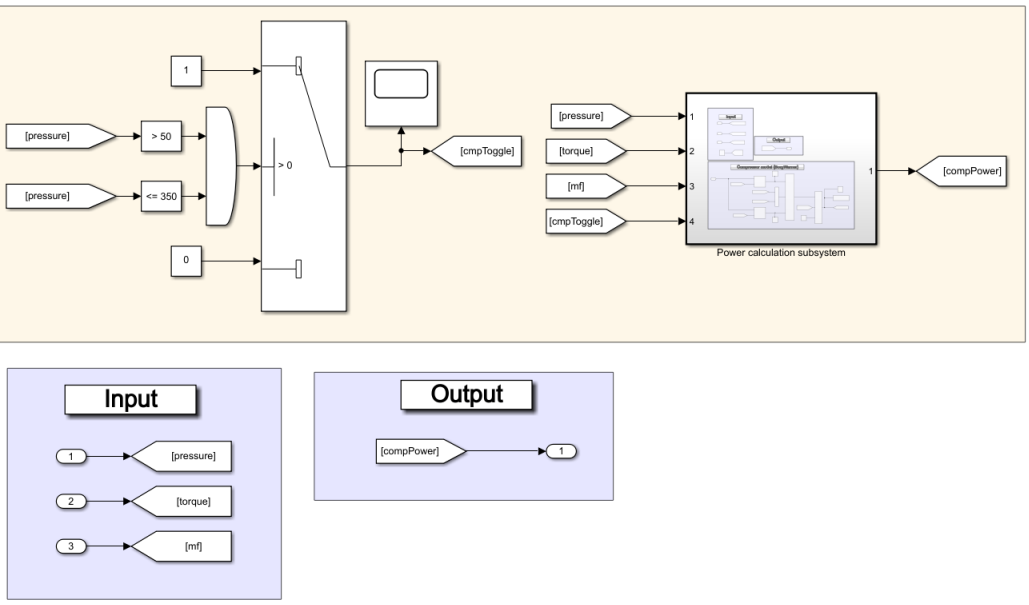

Figure 3.20: Compressor operation strategy implemented in HSS-GSP

- while tank pressure is above 350 bar, stage is 1
- if tank pressure is between 250 and 350 bar and the engine load at this time-step is low, stage is 1
- if tank pressure is between 250 and 350 bar and the engine load at this time-step is high, stage is 2
- if tank pressure is lower than 250 bar, stage is 3

In the case of Compressor 1 strategy, before the bank pressure drops below 350 bar, the secondary pipeline is used in both Compressor 1 and Compressor 2 configurations Therefore, the bank feeds the engine directly, bypassing the compressor/buffer system. In the case of Compressor 2, once the pressure limit is met, the main pipeline is constantly used until the end of the simulation and the buffer is assumed to remain in charged state throughout the simulation. Since Compressor 1 has more limited capabilities than Compressor 2, the need arises to establish a more complex gas path in the HSS, otherwise the engine requirements in terms of flow rate and pressure would not always be met. Therefore, in the case of Compressor 1, the main pipeline starts being used once the pressure limit is met, with the parallel recharging/discharging of the buffer, as described previously. Apart from the buffer recharging technique, which does not account for any usage in the main pipeline, the difference in the case of Compressor 1 is that, until the bank meets 250 bar pressure, the secondary pipeline is used to cover low engine loads. That means that, between 350 and 250 bar, the gas path alternates between the main and secondary pipeline depending on the engine load. Figure 3.21 depicts the implemented strategy in the case of Compressor 1. The limits of 350 and 250 bar are elected in order for losses to be accounted for and the engine to be able to receive the assumed injection pressure, for high and low loads, of 300 or 200 bar, respectively. These losses of 50 bar correspond to the route from the gas bank to the engine and they are mainly attributed to expansion. The purpose of the regulator just before the engine is to be able to alternate between the two pipelines and is a component consisting of a

Buffer cycling range: 310-350 bar	pressure range **Bank**	**Load** (1 = high & 0 = low)	**Compressor 1 active** (0: inactive, 1:active)
stage 0	>350	0&1	0
stage 1	250-350	0	0
stage 2	250-350	1	1
stage 3	50-250	0&1	1

Figure 3.21: Stages are defined by tank pressure level and engine load

valve system responsible to deliver gas to the engine.

4
Results

4.1 General comments

The general findings of simulations performed on Volvo proprietary drive-cycles are presented in this section. In order to protect sensitive information, some of the variables such as distance or power have been normalized. The dimensionless form was obtained for these two variables by dividing them with their corresponding maximum value throughout all cycles. The results produced in this chapter utilized 3 different drive-cycles that are integrated in GSP. For intellectual property reasons the drive-cycles shall remain unnamed, although data describing the general properties of these cycles shall be presented, since this will make the figures easier to examine, as well as provide some background so that conclusions can be drawn. Figures 4.1, 4.2 and 4.3 illustrate the properties of the different drive-cycles implemented. Uphill drive-cycle is a very intensive cycle with a very significant percentage of its route consisting of inclined road, especially going uphill. Light and Normal drive-cycles are very similar regarding the percentage of inclined road the vehicle encounters, with their main difference being that the inclination on Normal cycle variates more abruptly, constituting the Light cycle the easiest of the three cycles studied and simulated. Therefore, "normal" and "light" refer to the drive-cycle intensity in terms of inclination differences encountered in the route, which, in turn, translates to engine load. Having introduced the main drive-cycles relevant to the simulations performed, it is useful to mention a variable that strongly influences the fuel consumption. This variable is gross combination weight (GCW) and it is the gross weight of the vehicle plus the load. Once again, since these scalars constitute sensitive information for Volvo Group, the exact GCW values are withheld. However, the order of magnitude of the GCW values is several tens of tonnes.

4.2 Drive-cycles presentation

The results discussion will focus on the 3 drive-cycles that were described above, since it is assumed that they are capable of providing general insight on what may be encountered in a wide range of driving conditions. The figures presented in this section aim at providing a general idea of the properties and the results expected in each route. All variables except tank pressure and temperature are provided in a normalized manner, in order to protect company IP. The normalized variables, which are total hydrogen mass, engine flow rate, brake torque and compressor power were normalized with their corresponding max value encountered in all 3 cycles.

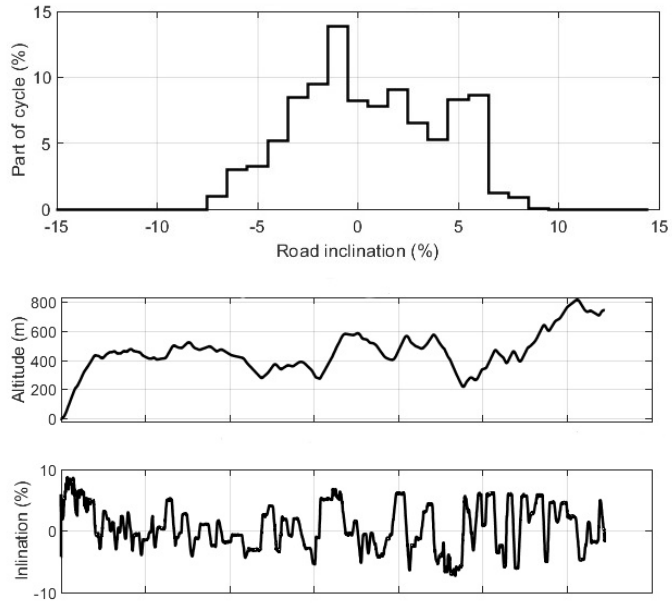

Figure 4.1: Road data for Uphill drive-cycle

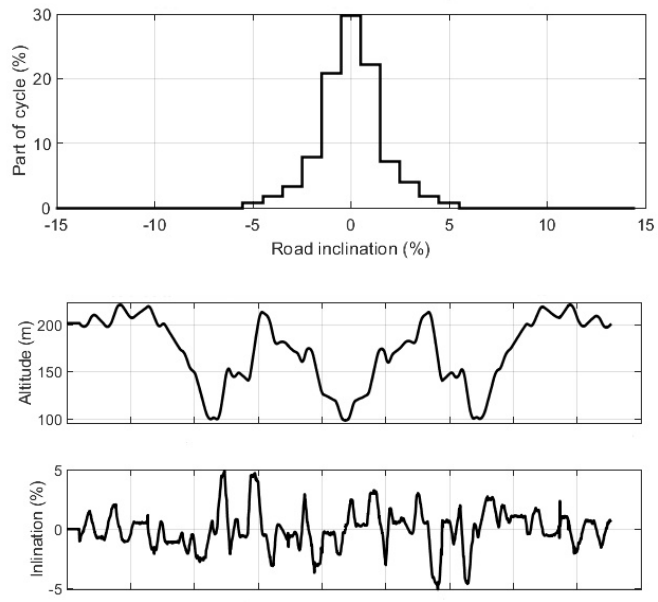

Figure 4.2: Road data for Light drive-cycle

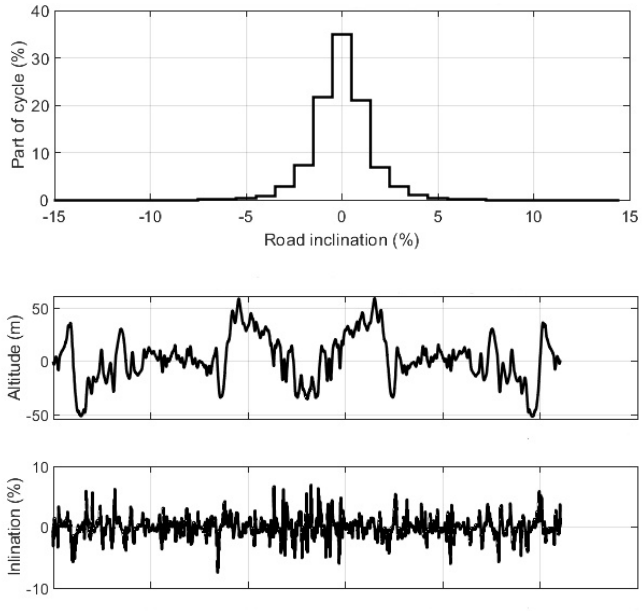

Figure 4.3: Road data for Normal drive-cycle

Since the results shown in this section all assume isothermal tank discharge, 11% remaining hydrogen mass is the maximum fuel utilization achieved in all 3 routes. This hydrogen quantity corresponds to 50 bar pressure in the tank, which is assumed to be the cut-off value, below which the tanks are considered "empty". Further simulations results along with the rest of the configurations and discharge processes will be reported later in the Results chapter, but, for simplicity and introduction to the simulations, Figure 4.4, Figure 4.5 and Figure 4.6 are considered sufficient.

For every route, the gas compressor begins its operation once the tank pressure hits 350 bar, which corresponds to around 61% tank state of charge. This means that only 39% of the fuel mass is consumed before the compressor becomes necessary to match the demanded injection pressures. The Uphill DC (drive-cycle) is the most demanding of the 3, judging from the road profile depicted in Figure 4.1, since the altitude climb is around 700 meters, much more than the other 2 routes. Another reason the Uphill is the most demanding of the 3 DC's is that it incorporated the highest cargo weight. This can also be observed from the average fuel flow rate, which is 58% of the maximum value, and the cycle-average compressor power, which is 13% of the overall maximum value. For comparison, the cycle-average compressor power for the Light and Normal DC is 5 and 4%, respectively. The calculation of the cycle-average compressor power refers to the whole cycle, including the initial stage when the compressor is inactive, as its title suggests. The brake torque plots appear to receive negative values in all routes. This can be explained by the fact that torque measurement includes engine braking and these values are included in the DC properties provided by Volvo Group.

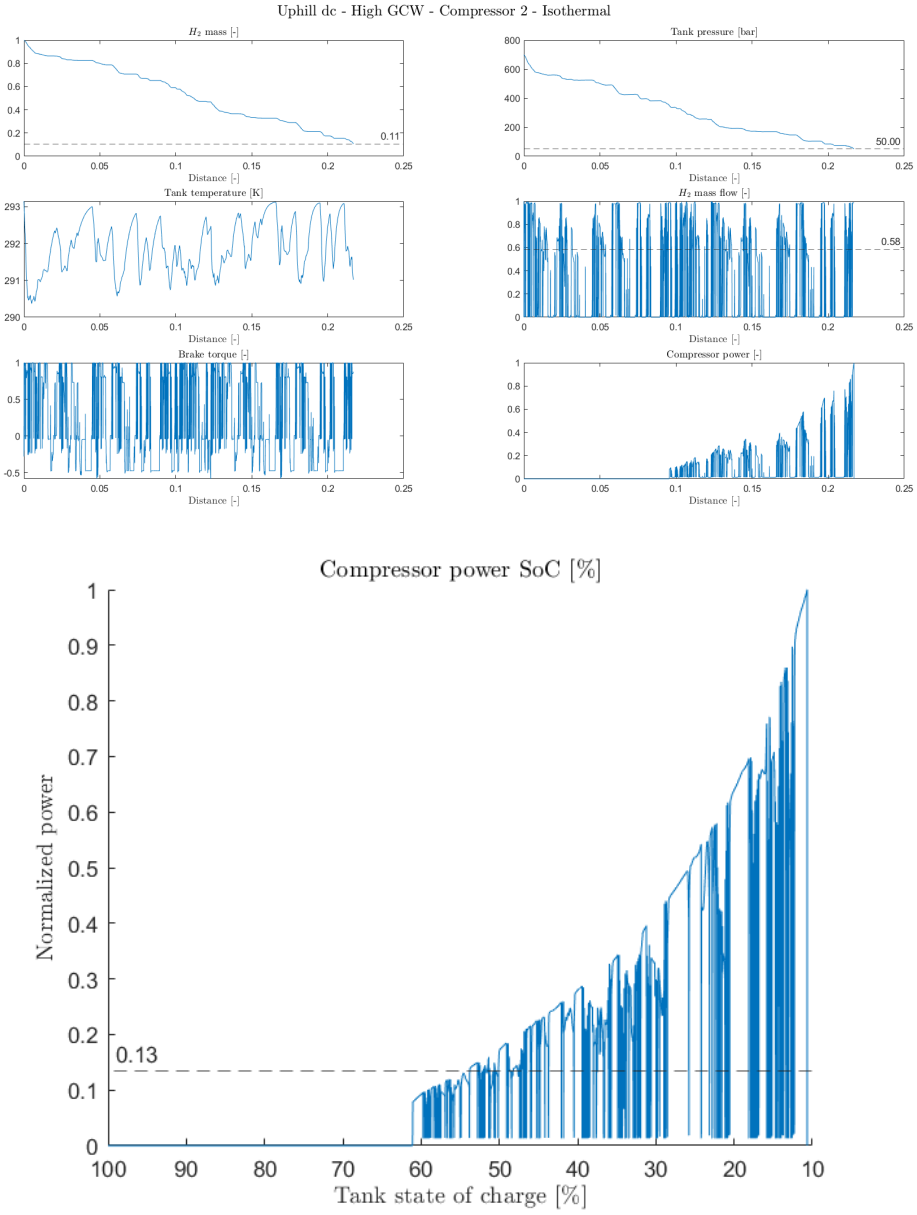

Figure 4.4: Uphill drive-cycle - High GCW - Isothermal discharge - Compressor 2

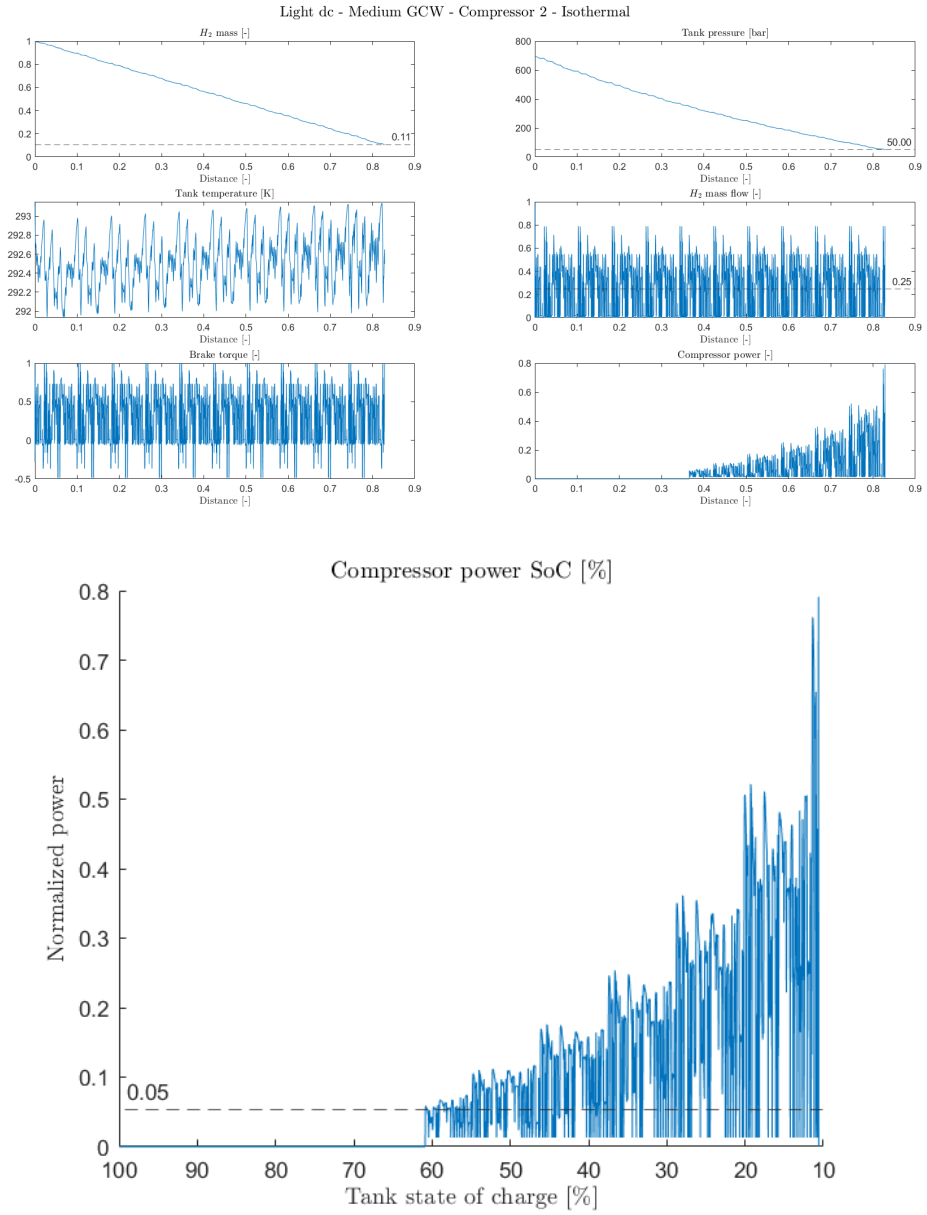

Figure 4.5: Light drive-cycle - Medium GCW - Isothermal discharge - Compressor 2

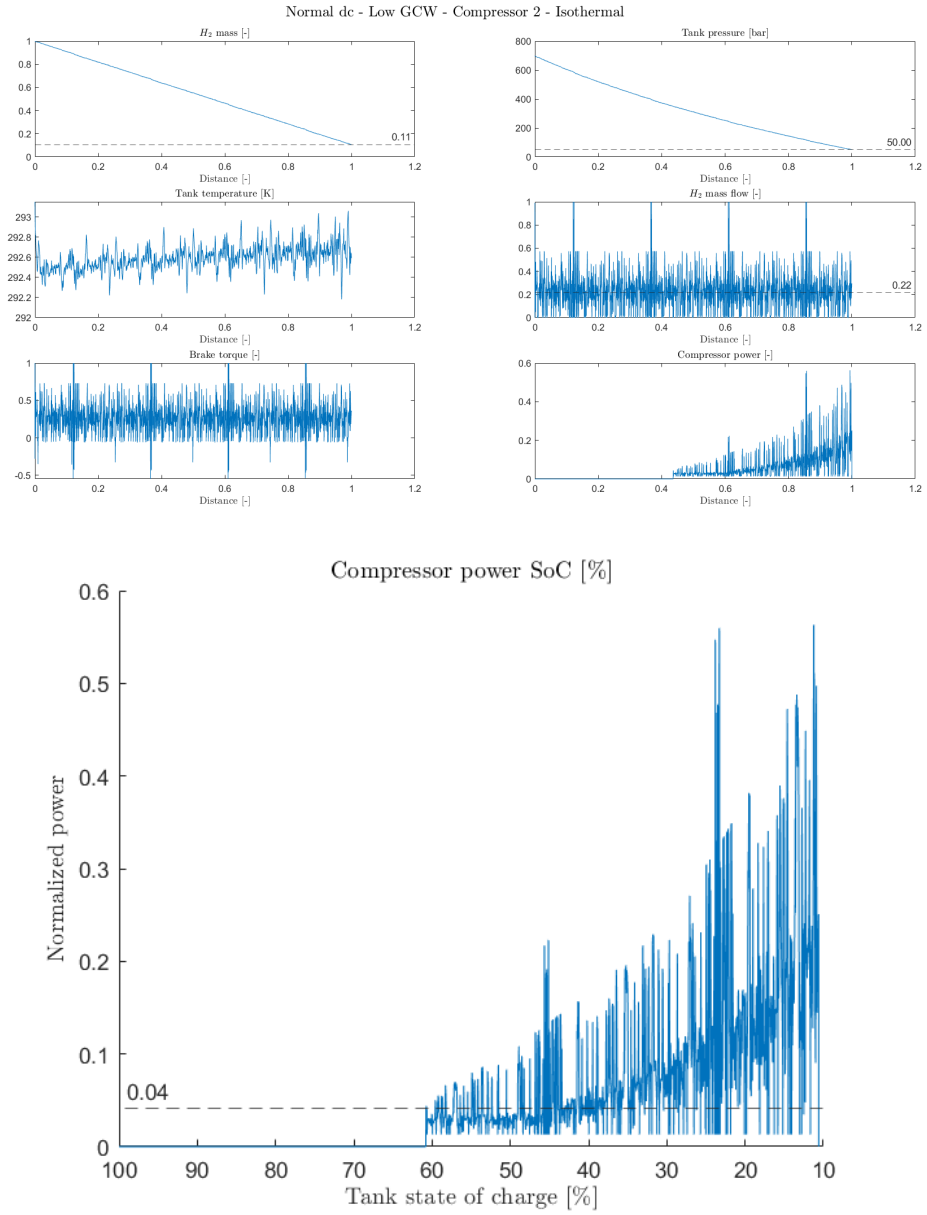

Figure 4.6: Normal drive-cycle - Low GCW - Isothermal discharge - Compressor 2

4.3 Effects of strategy

Before proceeding with the results, and having introduced the main configuration of the HSS in Figure 3.19, it is important to analyze in depth the different discharging techniques, with or without the compressor. Apart from the discharging process, which can be isothermal, adiabatic or real, the model also incorporates 4 different strategies to discharge the tanks and aim at achieving maximum driving distance with minimum parasitic losses. Parasitic losses refer to the auxiliary equipment that are assumed to drain power from the engine and as far as this thesis is concerned, on the basis of the powertrain, the only additional source of parasitic losses is the gas compressor.
It was always assumed that buffer recharging initiates when the buffer pressure falls below the target of 310 bar and does not stop recharging until it reaches 350 bar. The stages were given reference numbers in order to visualize the process and draw conclusions on which stage the simulation spends most of the time, depending on the drive-cycle and the discharging process. Figure 4.7 depicts the complete simulation implementing real heat transfer with Compressor 1, for the Uphill DC with high cargo weight. All variables presented in this figure are related to pressure, except for stage which represents the different pressure-load combinations as described in the bullet section above. Buffer recharging starts once the tank gas pressure reaches 350 bar, as expected. The detailed version of the recharging is presented in Figure 4.8, where it can be noted that the recharging is usually slower than the discharging, especially during intensive parts of the cycle where the buffer has to be used to cover the engine flow rate, while it is recharging. This specific simulation terminates with almost 200 bar remaining pressure in the main tanks. At this point, the buffer pressure in Figure 4.7 seems to fall below the lower limit of 310 bar, which dictates that the buffer is not able to cover the engine requirements in terms of fuel flow rate.

4.4 Effects of payload weight

The results presented in this section perform a comparison on the Uphill drive-cycle with different GCW implementation. As mentioned, the distance and the compressor power are presented in their normalized form and, in order to scale these values accordingly, the overall maximum of each of these two variables is obtained. The overall maximum distance value achieved was noted in the Normal DC with low GCW and isothermal discharge assumption, whereas the maximum compressor peak power was achieved on the Uphill DC with high GCW implementation and isothermal discharge assumption. Table 4.1 contains this information and the corresponding drive-cycles and their properties. With the Low GCW corresponding to the reference value, the Medium GCW case corresponds to 2x the GCW-reference and the High GCW corresponds to 5x the GCW-reference. An indication of the way in which fuel consumption varies with GCW is provided in a normalized form in Figure 4.9 where significant differences can be observed. This is a very broad indication concerning the expected values for gross weight and the results provided

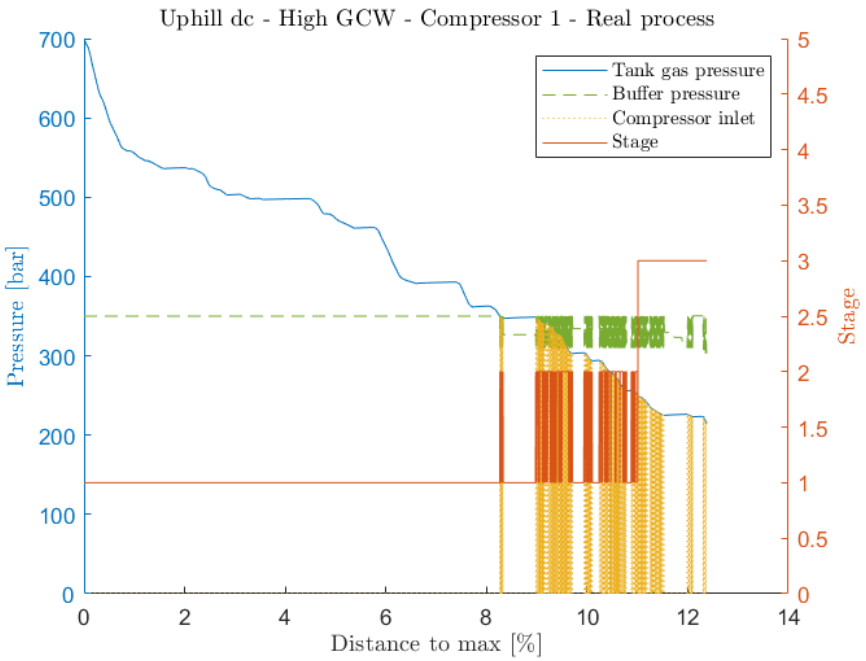

Figure 4.7: Gas pressure as a function of distance. The compressor inlet pressure matches the tank gas pressure when buffer is recharging.

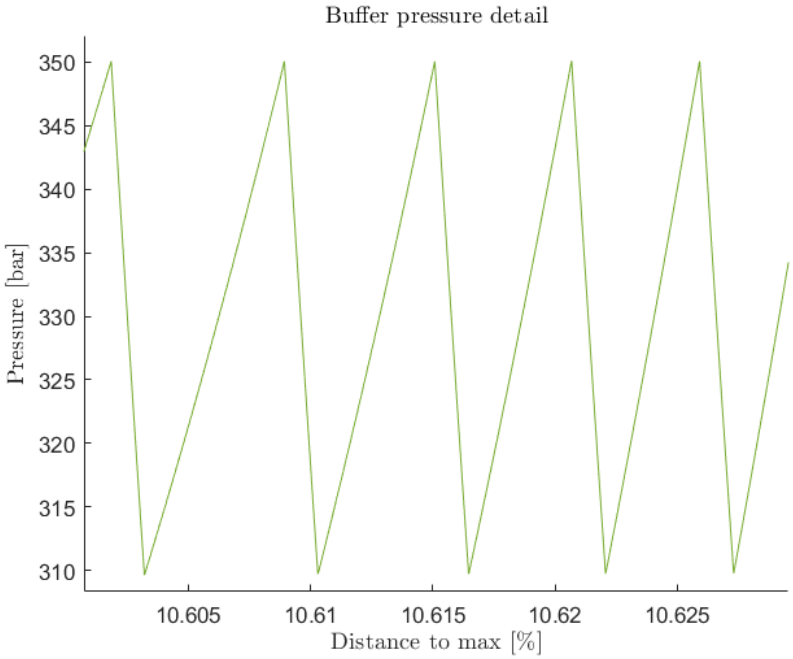

Figure 4.8: Buffer pressure as a function of normalised distance. Buffer recharging is much quicker than the discharging.

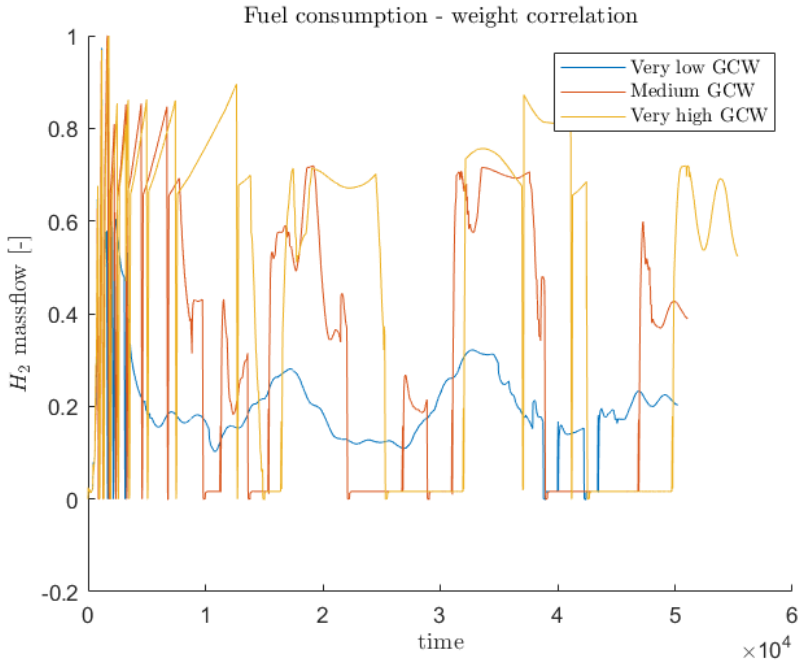

Figure 4.9: Normalised hydrogen massflow for different cargo weight implementations. Higher GCW can raise fuel consumption up to 3 times in certain parts of the drive-cycle.

Maximum values	**Drive-cycle**	**Process**	**GCW**
Distance achieved [-]	Normal	Isothermal	Low
Compressor power consumption [-]	Uphill	Isothermal	High

Table 4.1: The drive-cycles used to obtain dimensionless values

in Figure 4.9 only refer to a small percentage of the route. Typically, initial stages of drive-cycles tend to have elevated consumption due to acceleration. The average consumption might not exhibit such deviation from low to high GCW, although it is still significant.

In the context of the simulations performed for this thesis, the only weight-related results presented will be with the Uphill DC, paired with Compressor 2 and discharge implemented as real process. With these properties, results from two different cargo weights are compared and discussed. Figure 4.10 compares the two cases by normalising the values by the overall maximum obtained values, as shown in Table 4.1. The Low GCW case achieves significantly larger range, around 52% of the maximum, compared to the 22% achieved by the High GCW case. Gas temperature drop is steeper for the High GCW case, which can be explained by the fact that mass and, therefore, pressure drops faster as well.

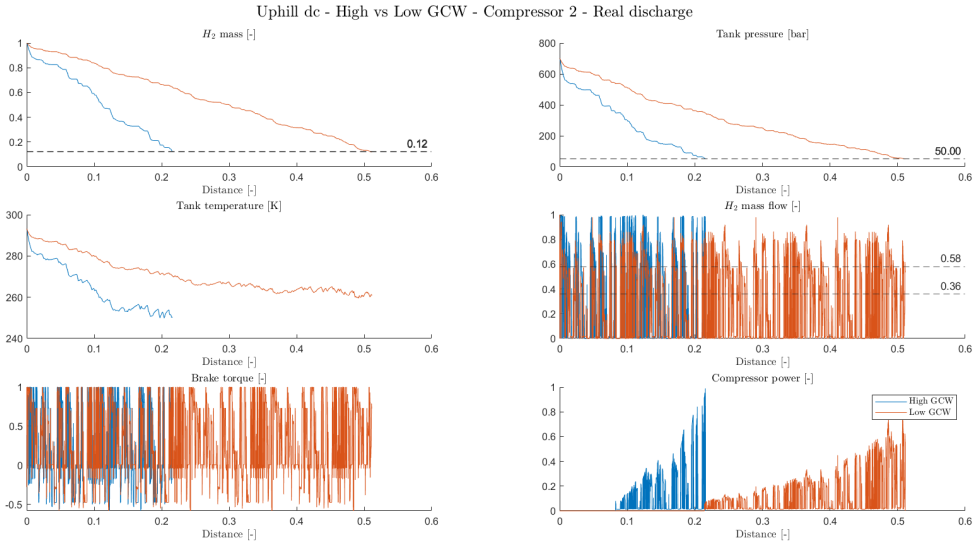

Figure 4.10: Comparative data for uphill drive-cycle with two different payload configurations. Significant range advantage is noted on the Low GCW implementation.

4.5 Effects of the inner convection coefficient

In Figure 4.11, the minimum heat transfer coefficient value towards the end of the cycle is very similar for the two cases simulated. Heat transfer coefficient depends on Nusselt number, thermal conductivity and characteristic length. Characteristic length is the same for every simulated case since it is a geometrical property connected to the tank. Thermal conductivity depends on temperature and Nusselt number depends mainly on Rayleigh number, which is a function of multiple other variables.

Figure 4.12 depicts the gas, inner wall and outer wall temperatures for the Low and High GCW cases. The upper part of the plot refers to the Low GCW case, in which temperature is retained higher compared to the High GCW case, due to the slower discharge of fuel, slower temperature drop and hence more time for the heat transfer from the ambient to the colder gas. This allows more heat to be transferred to the fuel, hence higher temperature to be maintained. The temperature trend depicted places the gas temperature lower, the inner wall temperature follows and, lastly, the outer wall temperature. This trend can be explained by the fact that the inner and outer walls appear to have some delay in sensing the gas temperature drop and it is in line with what the heat transfer mechanism applied. In Figure 4.13 the gas temperature and pressure is presented for the "real discharging process" for the case of GT against the developed Simulink model, the so-called "GSP". There is a maximum gas temperature difference of 18K, with the Simulink model over-predicting the temperature and, thus, under-predicting heat transfer. Under-prediction of the heat transfer means that the inner heat transfer coefficient has been under-predicted with the value of 5 $W/m^2/K$.

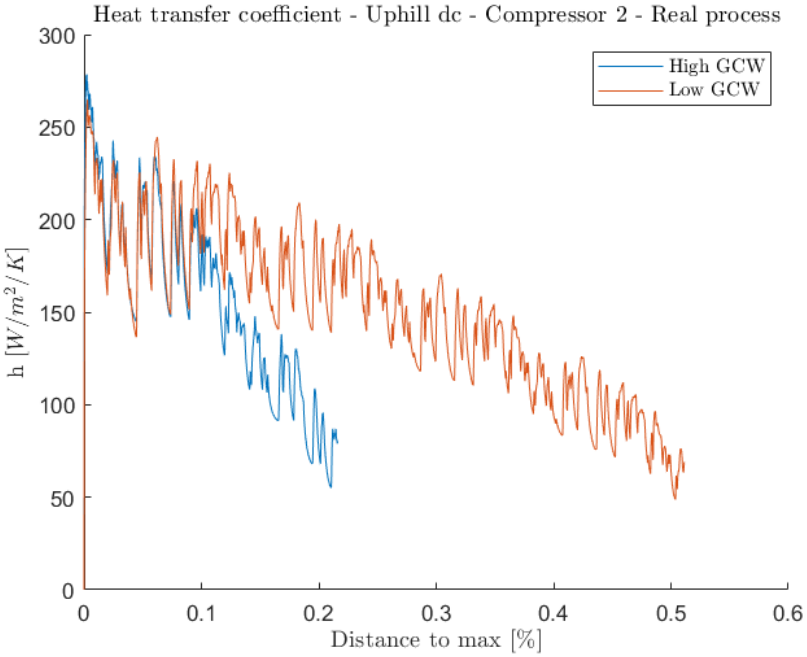

Figure 4.11: Heat transfer coefficient as a function of normalised distance. Minimum inner heat transfer coefficient is similar for the two different payloads.

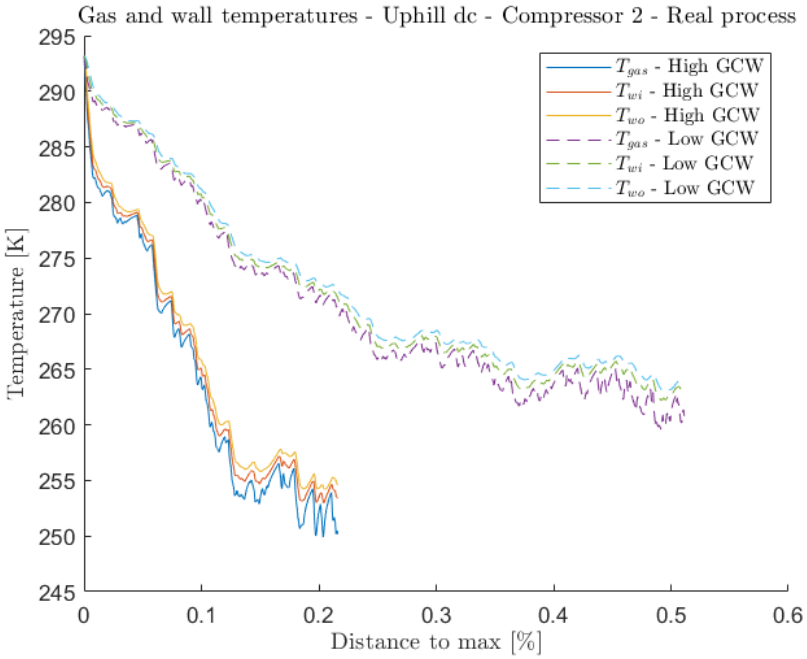

Figure 4.12: Gas and wall temperatures as a function of driving distance. Inner and outer wall temperatures follow the gas temperature trend for both cases.

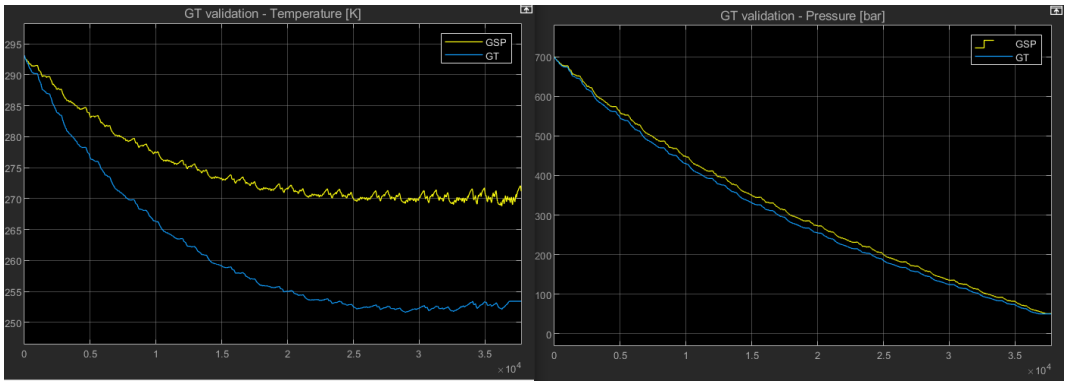

Figure 4.13: Gas temperature and pressure as a function of time (plots retrieved from Simulink model). Gas temperature differs by a max of 18K - $h_{inner} = 5\ W/m^2/K$

4.6 Effect of external convection coefficient

As mentioned in Section 3.3.2, the modelled heat transfer mechanism applied does not include analytical calculations of the external heat transfer coefficient. For this reason, a range of values was tested and the simulation results will be presented and discussed in this section.

All of the simulations performed for this thesis used a constant value of 5 $W/m^2/K$ for the external convection coefficient and the results presented throughout this report refer to this value, except for this section. The simulation tests performed in this section used the simple discharge method, which does not assume any compressor and uses the tanks until they reach 350 bar pressure. This method was selected as the simplest and quickest method to provide insight on the effect the external convection coefficient has on the range achieved. Figures 4.14, 4.15 and 4.16 depict the distance-to-max achieved with 3 different values of external convection coefficients and for the isothermal discharge process implementation which assumes an overall heat transfer coefficient of $10^5\ W/m^2/K$. Distance-to-max represents the range covered by the vehicle in relation to the overall maximum distance achieved by any GCW, DC or discharge process, combined. Other values tested for the external heat transfer coefficient are 20 and 100 $W/m^2/K$. In all 3 drive-cycles tested, the coefficient value that causes the most significant deviation in terms of the range achieved is the smallest one, 5 $W/m^2/K$. For the other 2 coefficient values, the range does not deviate significantly, especially with the value of 100 $W/m^2/K$. Studies performed both during filling and emptying of hydrogen tanks, report a constant value of 6 $W/m^2/K$ for the external convection coefficient in Type IV gas tanks, which is similar to the value used in the simulations of this thesis [8], [32]. The value used for the external convection coefficient of $h = 5\ W/m^2/K$ is also chosen based on the GT-Power simulation results compared to the test data from the literature.

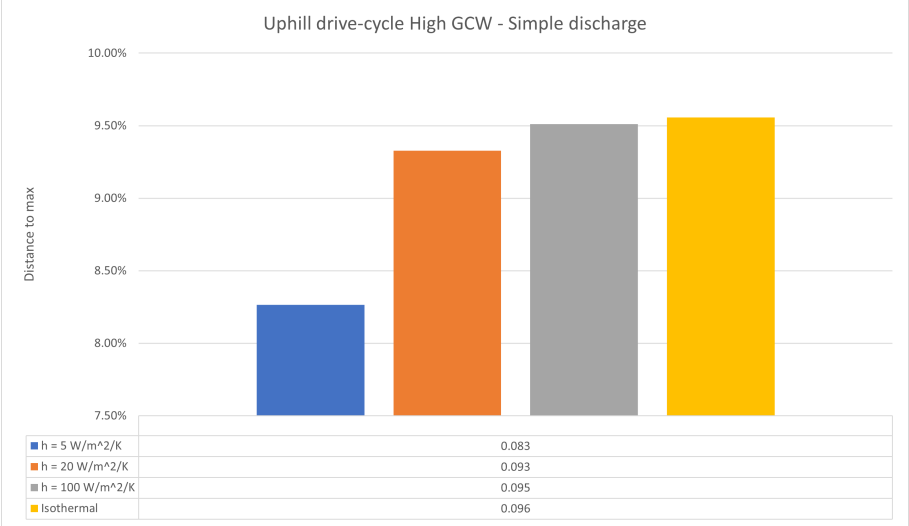

Figure 4.14: Uphill DC external convection coefficients test

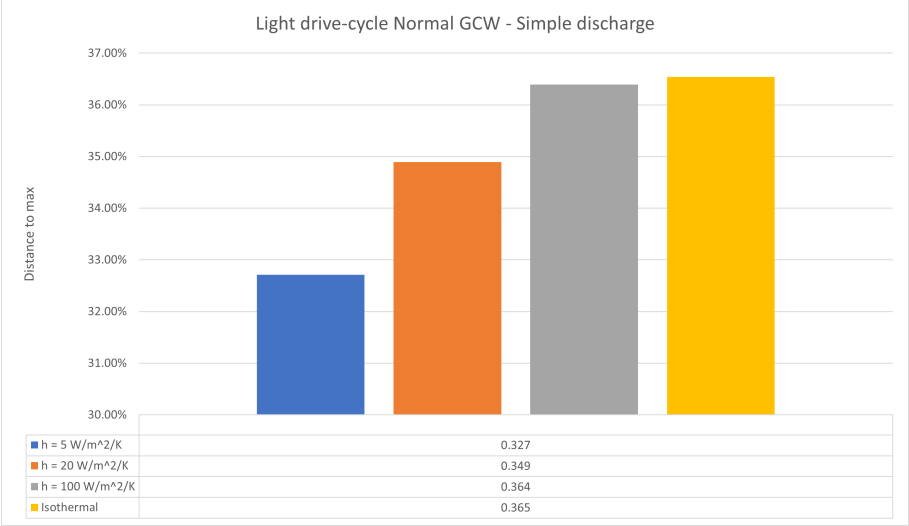

Figure 4.15: Light DC external convection coefficients test

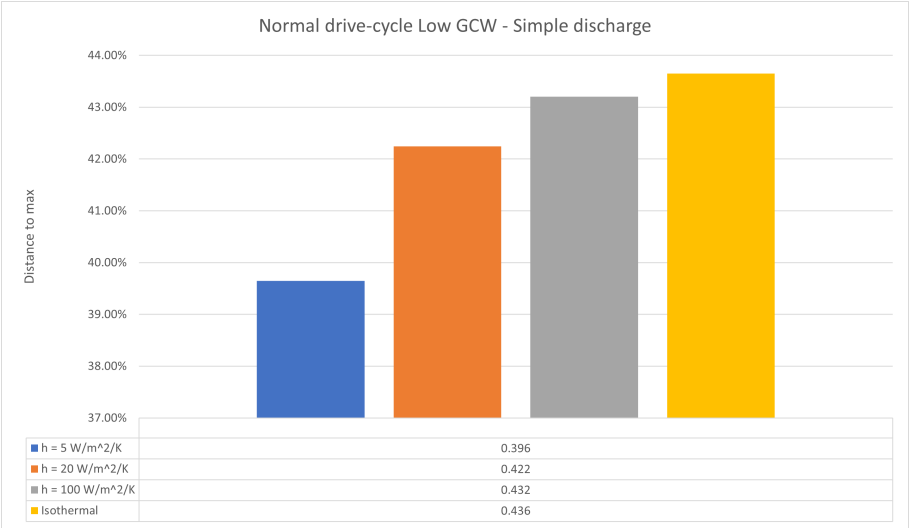

Figure 4.16: Normal DC external convection coefficients test

4.7 Compressor power estimation

The model currently assumes the use of a reciprocating mechanical compressor. The engine is assumed to provide the necessary power for the compressor to operate, thus one may think of the compressor as an energy sink or a parasitic loss segment in our model.
Figures 4.17, 4.18 and 4.19 present the parasitic losses for all 3 drive-cycles, with all discharge process implementation and all strategy configurations. With simple discharge, parasitic losses are zero for all cases, since the compressor is inactive throughout the simulation. There is an extra segment in the figures presented in this section, named "SMART STRATEGY" and it constitutes the strategy developed within Volvo Group. For reasons connected with intellectual property protection, the details and methods governing this strategy cannot be revealed, but the results are posted here for reference. The parasitic losses calculation in the figures provided in this section, is described in (4.1). Compressor power is calculated through data provided for the 2 compressor configurations, whereas torque and engine speed are given by the GSP. In order to calculate the parasitic losses, the cycle-average values of both the compressor power and the denominator's product are calculated for each time-step in the model.

$$\text{parasitic losses} = \frac{\text{mean}\left(\text{compressor power}\right)}{\text{mean}\left(\text{torque} \cdot \text{engine speed}\right)} \cdot 100\% \tag{4.1}$$

In all drive-cycle cases, the isothermal discharge showed the lowest losses, followed by the real discharge process and the adiabatic. This trend is expected from theory, since the pressure is held higher for the isothermal discharge which means that more percentage of the drive-cycle can be completed before the compressor starts operating. Apart from that, once the compressor does start operating, higher pressure means that less power is required to bring the injection pressure to the required levels and, thus, lower parasitic losses are exhibited in this case. For the Uphill DC,

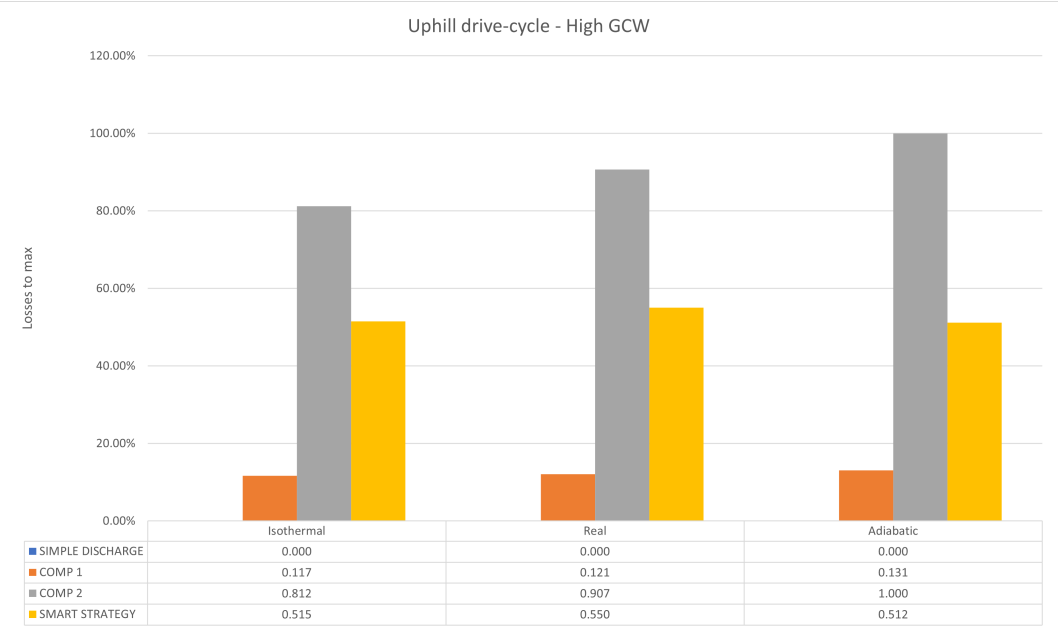

	Isothermal	Real	Adiabatic
SIMPLE DISCHARGE	0.000	0.000	0.000
COMP 1	0.117	0.121	0.131
COMP 2	0.812	0.907	1.000
SMART STRATEGY	0.515	0.550	0.512

Figure 4.17: Normalised parasitic losses - Uphill DC

	Isothermal	Real	Adiabatic
SIMPLE DISCHARGE	0.000	0.000	0.000
COMP 1	0.237	0.298	0.408
COMP 2	0.781	0.844	0.965
SMART STRATEGY	0.684	0.722	0.779

Figure 4.18: Normalised parasitic losses - Light DC

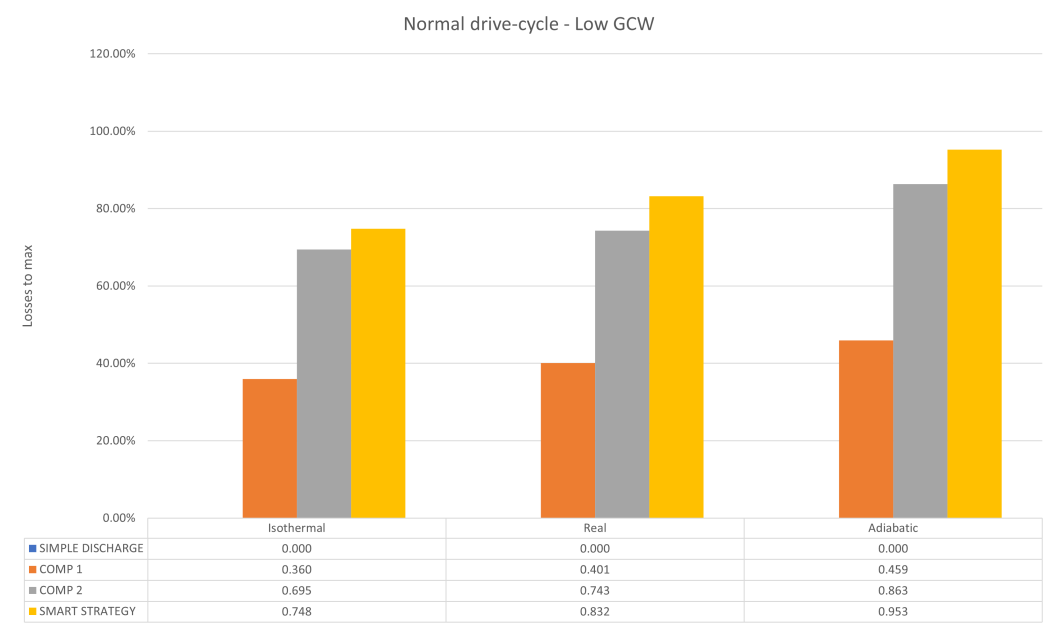

Figure 4.19: Normalised parasitic losses - Normal DC

the configuration incorporating Compressor 2 presents the largest parasitic losses, amounting to 90 to 100% of the max losses, whereas the smart strategy exhibits losses of about 50% of the overall maximum value. The same trend is true for the Light DC, with the smart strategy showing values closer to the Compressor 2 simulations. The only drive-cycle in which smart strategy gives greater losses is the Normal DC with Low GCW. This irregularity stands because the smart strategy is a set of rules that ideally would be able to adapt to the drive-cycle encountered, but this thesis focused on developing an all around package that can cope with most of the duty cycles that might be encountered. The parasitic losses connected with Compressor 1 are very low in all cases, showing ranges of 10 to 45%. This information is not sufficient to judge whether Compressor 1 is the most suitable for the purposes of this study, since the driving range has to be studied in parallel with the losses in order to draw firm conclusions. Figure 4.7 is an example of this behaviour, as the simulation is terminated with upwards of 200 bar of remaining pressure, as Compressor 1 is not able to meet the engine flow rate. For this purpose, Figures 4.20, 4.21 and 4.22 are presented here as well.

In the Light and the Normal drive-cycles, Compressor 1 configuration might be an appealing choice as, in many cases, it achieves comparable range to the Compressor 2 or the smart strategy configurations, with much smaller losses. This statement is not true for the Uphill drive-cycle, where the range achieved with Compressor 1 is close to half of what the Compressor 2 or smart strategy configurations achieve. In this case it would be much simpler and economic to apply the simple discharge without the need for a gas booster and an elaborate mechanism that would apply complex sets of rules. Compressor 2 range advantage is visible throughout the different drive-cycles, although in the case of the Normal drive-cycle, the results are comparable with every configuration except for the simple discharge.

It is difficult to definitely state that one strategy is advantageous over another one,

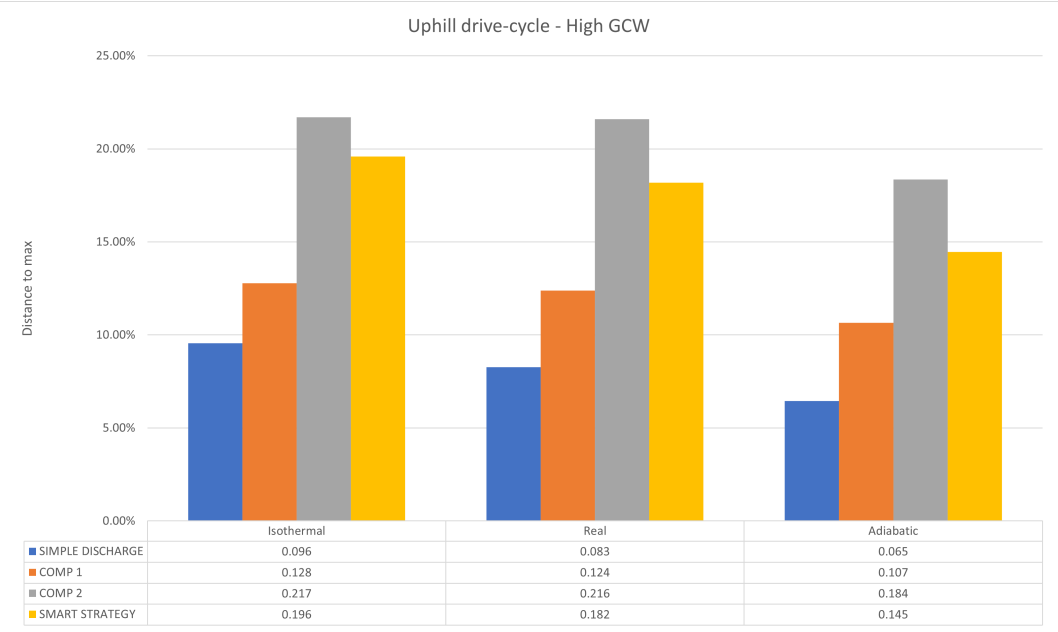

	Isothermal	Real	Adiabatic
SIMPLE DISCHARGE	0.096	0.083	0.065
COMP 1	0.128	0.124	0.107
COMP 2	0.217	0.216	0.184
SMART STRATEGY	0.196	0.182	0.145

Figure 4.20: Normalised range achieved - Uphill DC

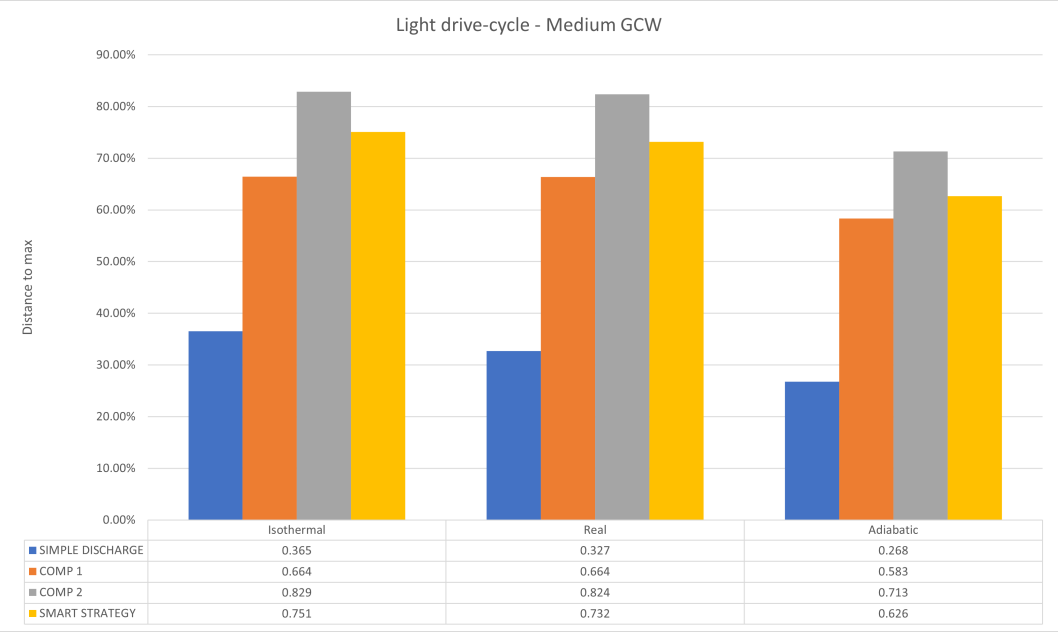

	Isothermal	Real	Adiabatic
SIMPLE DISCHARGE	0.365	0.327	0.268
COMP 1	0.664	0.664	0.583
COMP 2	0.829	0.824	0.713
SMART STRATEGY	0.751	0.732	0.626

Figure 4.21: Normalised range achieved - Light DC

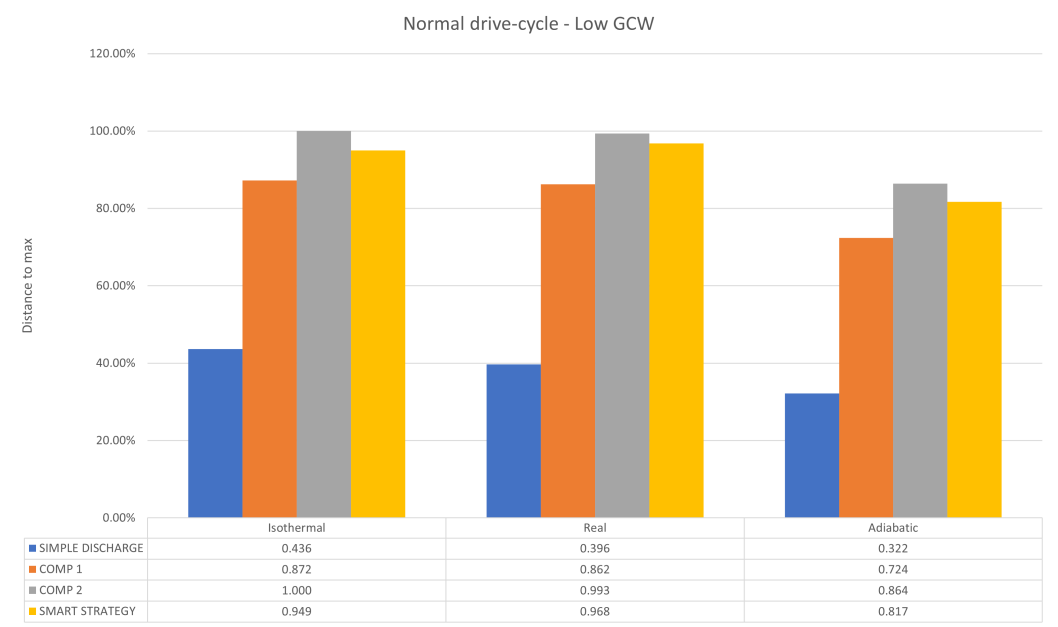

Figure 4.22: Normalised range achieved - Normal DC

since this is strongly connected with the drive-cycle and cargo weight combination implemented for each route. The selection of the compressor size and HSS operating strategy will depend on the applications that any particular truck is planned to be used in. Thus, a careful techno-economic assessment will have to be performed before making the selection.
The cases provided here are assumed to be compared in a direct manner. Direct comparison means that it is clear which configuration required more compressor power and how much more. Although the peak power achieved by the compressor defines its size and capabilities, the average power is also a very important quantity because it dictates the mean mechanical energy the compressor will require during its operation. It is always the case that higher GCW configurations and adiabatic discharge process yield higher average compressor power and, thus, parasitic losses for the system as a whole. It should be noted that the parasitic losses refer to the whole of the cycle, so it takes into account the initial stage of the simulations when the compressor is inactive.

4.8 Effects of the drive-cycles

In this section, pressure and compressor power will be discussed for all 3 drive-cycles and the different strategies implemented. In order to maintain simplicity and make figures more understandable, only results connected with real discharging process will be presented. This choice is also supported by the fact that the "real discharging process" is attempting to reflect how the tanks would discharge in a realistic scenario. Figures 4.23, 4.24 and 4.25 show the tank pressure as a function of the normalised range achieved in the simulation. In the case of Compressor 1, where a buffer tank was also used, in Figure 4.23, the buffer pressure variation is also presented.

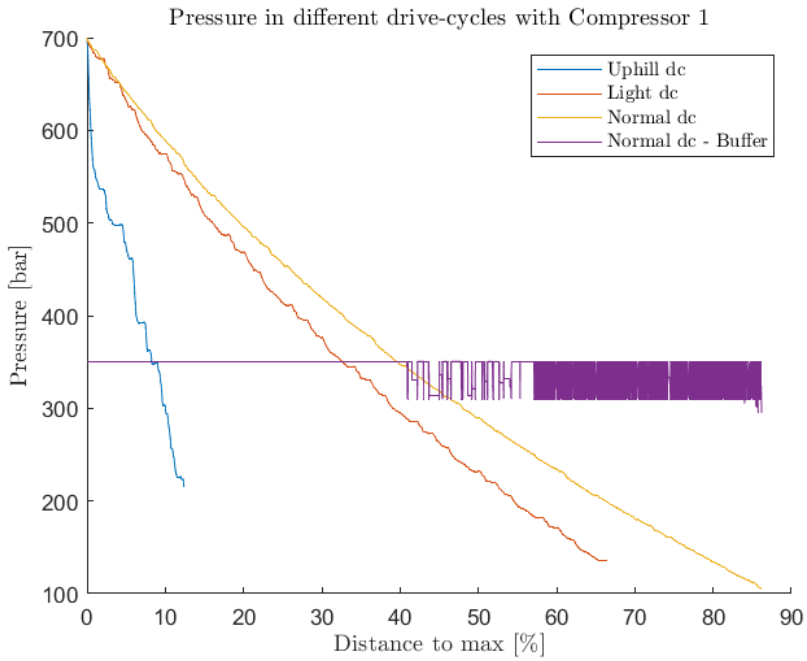

Figure 4.23: Compressor 1 implementation includes buffer pressure variation

In Figure 4.24, with Compressor 2 implementation, it can be observed that tank pressure reaches similar values at the end of the simulation for each drive-cycle. On the other hand, this does not seem to hold with Compressor 1 where, in Figure 4.23 it can be seen that the Uphill drive-cycle terminates with the highest remaining pressure, followed by the Light drive-cycle and the Normal one. The explanation behind this inaccuracy is that Compressor 1 cannot provide enough mass flow rate and maintain the injection pressure. For the simple discharge case in Figure 4.25, final tank pressure is always 350 bar because there is no compressor and the model terminates the simulation once the pressure falls below 350 bar - the maximum required injection pressure. Throughout the different strategy implementations, it is a rule that the Normal drive-cycle achieves the higher range, followed by the Light drive-cycle and the consumption-intensive Uphill drive-cycle, which achieves the lowest range by far. The explanation behind the Light drive-cycle not achieving the longest range is that it incorporates medium cargo weight. If this cycle was tested with low cargo weight similar to the one in Normal drive-cycle, the results would be reversed. Out of all 3 strategies, the one using Compressor 2 provides maximum tank utilization, emptying the tanks down to the low limit of 50 bar. In terms of state of charge, this limit of 50 bar corresponds to approximately 89% tank utilization.

Figures 4.26 and 4.27 depict the compressor power for the different drive-cycles with the model using Compressor 1 and Compressor 2, for the real discharge process. Compressor 1 power consumption increases, moving from the Uphill drive-cycle to the Normal drive-cycle. With Compressor 2, on the other hand, the situation is reversed and moving from the Uphill drive-cycle to the Normal drive-cycle the normalised compressor power seems to receive continuously reducing values with

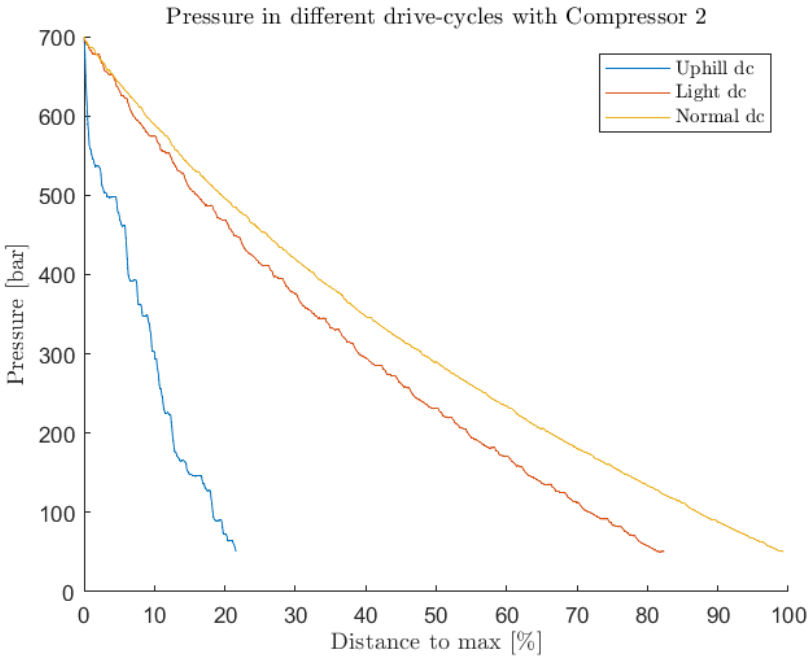

Figure 4.24: Maximum fuel utilization achieved with Compressor 2, emptying the tanks down to 50 bar

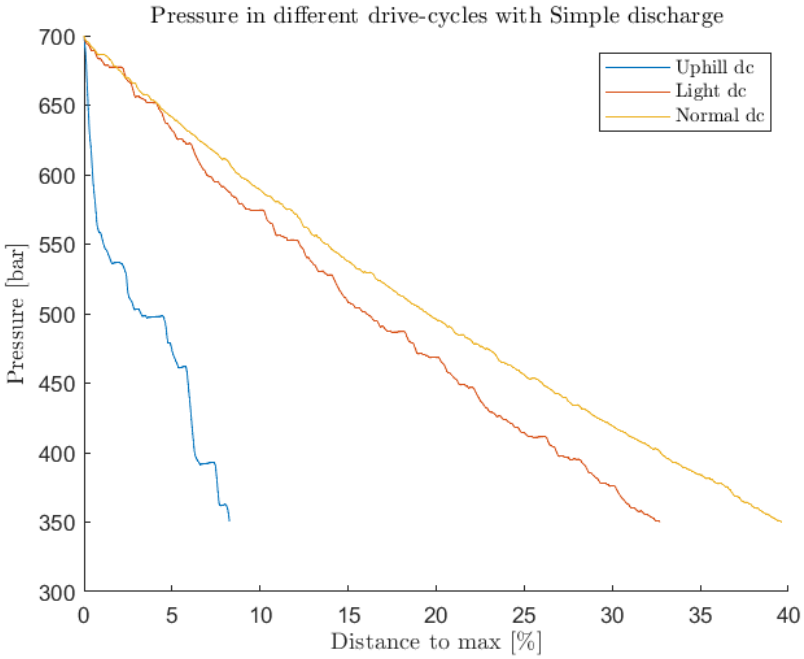

Figure 4.25: Simple discharge set of rules imposes simulation termination at 350 bar tank gas pressure

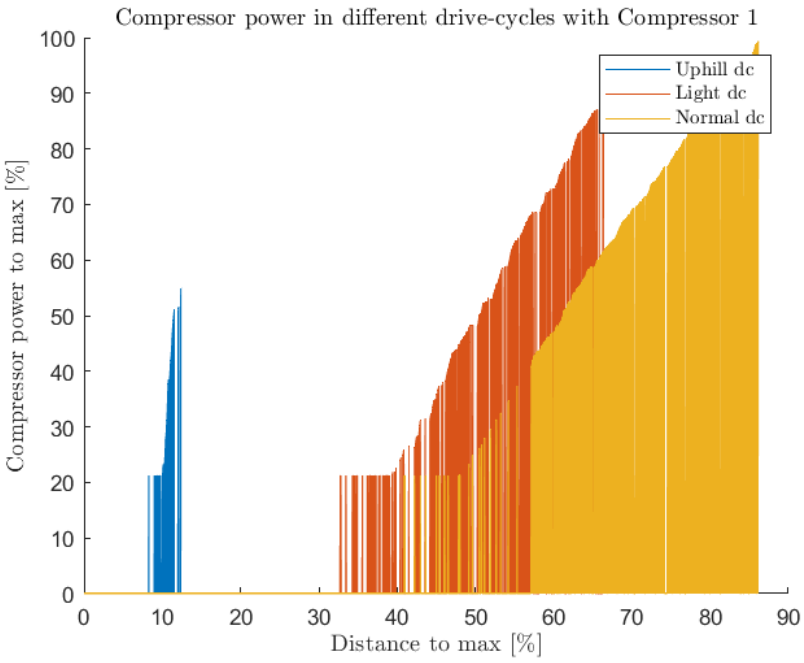

Figure 4.26: Compressor 1 achieves limited range in the Uphill drive-cycle - limited power consumption exhibited as well

lower peaks. The two gas compressor systems exhibit opposing behaviour looking at the normalised power consumption from one drive-cycle to another. Again, this fact alone is not enough to draw firm conclusions and the range achieved in each case has to be examined as well. Despite that, it is safe to assume that Compressor 1 is not a suitable choice for the Uphill drive-cycle, since the compressor only operates for a limited amount of the cycle and, in combination with the bar plots of Figure 4.20, it is clear that this assumption stands. The compressor power exhibits a steep increase with the distance travelled and the trend is also non-linear. This shows that increasing the vehicle range results in the increasingly large parasitic loss and penalty on the powertrain efficiency, as well as requires increasingly larger compressor size. This observation is also in agreement with the results presented in Section 4.7 and specifically Figures 4.17, 4.18 and 4.19. The parasitic power figures show very large fluctuations, and peaks do not tend to last for prolonged periods of time. This suggests that a smaller compressor with lower mass flow rate capacity, and hence smaller maximum power consumption, can be used in combination with a buffer tank. In such scenario, the peaks in the fuel flow demand can be covered by discharging the buffer tank, while compressor would recharge it during the periods of lower demand which are more prevalent, thus simultaneously allowing to reduce the parasitic losses and meet the engine fuel flow demand at all times.

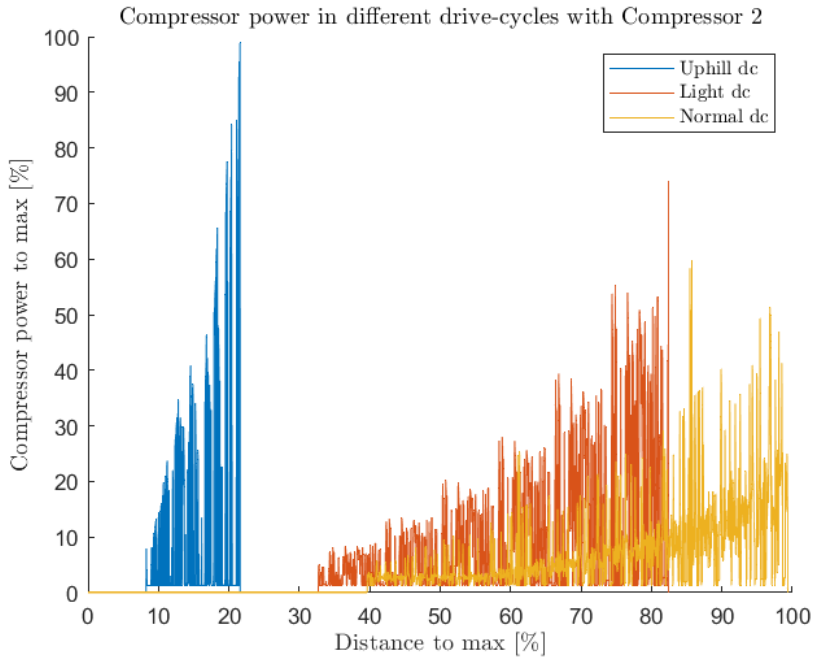

Figure 4.27: Similar normalised power consumption estimated for the Light and Normal drive-cycles

5
Future work

At this point, there are indications regarding the capabilities and general properties of the HSS and the compressor, since the model explores the complete working range. These indications point to the suitable strategy that should be implemented, depending on the route and the vehicle configuration. This was partly achieved by setting up the 2 extreme discharging processes governing the discharging and receiving an indication through GT regarding which one best describes a realistic scenario. Also, various factors were studied in the *Results* chapter, such as strategy, payload weight, convection coefficients, compressor power requirements and drive-cycle encountered. Since it was found that the compressor choice plays a significant role in the range achieved by the vehicle, it is suggested that future work focuses on gathering compressor map data from multiple companies or assuming different compressor sizes. This will point to the optimal design of the HSS, taking into account the dependencies mentioned previously and studied in *Results*. Below follows a list of the most important steps for future work:

- work towards developing a strategy that would adequately and conveniently fit all or most of the drive-cycles available in order to reduce the need to adapt complex sets of rules and mechanisms to the needs of the route
- exploring different discharging strategies is an essential part of this operation, since this will reduce the parasitic losses through the compressor and, in turn, increase the driving range achieved
- further work on the buffer tank development
- integrate a heat exchanger model into the system, since there will be a need for one, judging from the temperatures encountered during operation
- strive to calibrate against all relevant data available, which are limited
- connect the existing model with GT-Power, either by developing from scratch in GT or by coupling with the existing model
- perform engine performance simulations in GT-Power

Bibliography

[1] T. Abbasi and S. Abbasi, "'renewable' hydrogen: Prospects and challenges," *Renewable and Sustainable Energy Reviews*, vol. 15, no. 6, pp. 3034–3040, 2011.

[2] D. J. Durbin and C. Malardier-Jugroot, "Review of hydrogen storage techniques for on board vehicle applications," *International Journal of Hydrogen Energy*, vol. 38, no. 34, pp. 14595–14617, 2013.

[3] M. Hirscher and K. T. shi Aichi-ken Hirose, "Handbook of hydrogen storage : new materials for future energy storage," 2010.

[4] L. Zhou and Y. Zhou, "Determination of compressibility factor and fugacity coefficient of hydrogen in studies of adsorptive storage," *International Journal of Hydrogen Energy*, vol. 26, no. 6, 2001.

[5] S. S. Makridis, "Hydrogen storage and compression," 2016.

[6] "Hydrogen Tank: Doosan Mobility Innovation." `https://www.doosanmobility.com/en/products/hydrogen-tank/`. Accessed: November 2, 2023.

[7] S. M. Aceves, G. D. Berry, J. Martinez-Frias, and F. Espinosa-Loza, "Vehicular storage of hydrogen in insulated pressure vessels," *International Journal of Hydrogen Energy*, vol. 31, no. 15, 2006.

[8] L. Zhao, F. Li, Z. Li, L. Zhang, G. He, Q. Zhao, J. Yuan, J. Di, and C. Zhou, "Thermodynamic analysis of the emptying process of compressed hydrogen tanks," *International Journal of Hydrogen Energy*, vol. 44, no. 7, 2019.

[9] U. Bossel and B. Eliasson, "Energy and Hydrogen Economy," *European Fuel Cell Forum, Lucerne*, 2002.

[10] J. Q. Li, J. C. Li, K. Park, S. J. Jang, and J. T. Kwon, "An analysis on the compressed hydrogen storage system for the fast-filling process of hydrogen gas at the pressure of 82 mpa," *Energies*, vol. 14, no. 9, 2021.

[11] M. Gurz, E. Baltacioglu, Y. Hames, and K. Kaya, "The meeting of hydrogen and automotive: A review," in *International Journal of Hydrogen Energy*, vol. 42, 2017.

[12] A. Léon, *Hydrogen technology: mobile and portable applications ; with 50 tables.* 2008.

[13] F. Martins, C. Felgueiras, M. Smitkova, and N. Caetano, "Analysis of fossil fuel energy consumption and environmental impacts in european countries," *Energies*, vol. 12, no. 6, p. 964, 2019.

[14] P. M. Falcone, M. Hiete, and A. Sapio, "Hydrogen economy and sustainable development goals: Review and policy insights," *Current Opinion in Green and Sustainable Chemistry*, vol. 31, p. 100506, 2021.

[15] G. Li, "Optimization study of pilot-ignited natural gas direct-injection in diesel engines," *SAE transactions*, pp. 1739–1748, 1999.

[16] A. Boretti, "Hydrogen internal combustion engines to 2030," *International Journal of Hydrogen Energy*, vol. 45, no. 43, pp. 23692–23703, 2020.

[17] N. D. Miguel, R. O. Cebolla, B. Acosta, P. Moretto, F. Harskamp, and C. Bonato, "Compressed hydrogen tanks for on-board application: Thermal behaviour during cycling," *International Journal of Hydrogen Energy*, vol. 40, no. 19, 2015.

[18] K. Nasrifar, "Comparative study of eleven equations of state in predicting the thermodynamic properties of hydrogen," *International journal of hydrogen energy*, vol. 35, no. 8, pp. 3802–3811, 2010.

[19] R. Von Helmolt and U. Eberle, "Fuel cell vehicles: Status 2007," *Journal of power sources*, vol. 165, no. 2, pp. 833–843, 2007.

[20] N. D. Miguel, B. Acosta, P. Moretto, and R. O. Cebolla, "The effect of defueling rate on the temperature evolution of on-board hydrogen tanks," in *International Journal of Hydrogen Energy*, vol. 40, 2015.

[21] R. Immel and A. MacK-Gardner, "Development and validation of a numerical thermal simulation model for compressed hydrogen gas storage tanks," in *SAE Technical Papers*, 2011.

[22] G. Nellis and S. Klein, *Heat transfer*. Cambridge university press, 2008.

[23] J. Guo, J. Yang, Y. Zhao, X. Pan, L. Zhang, L. Zhao, and J. Zheng, "Investigations on temperature variation within a type III cylinder during the hydrogen gas cycling test," in *International Journal of Hydrogen Energy*, vol. 39, 2014.

[24] V. Molkov, M. Dadashzadeh, and D. Makarov, "Physical model of onboard hydrogen storage tank thermal behaviour during fuelling," *International Journal of Hydrogen Energy*, vol. 44, no. 8, 2019.

[25] C. Valve, "Flow of fluids through valves, fittings and pipe tp-410 metric," 1999.

[26] F. P. Incropera, D. P. DeWitt, T. L. Bergman, A. S. Lavine, *et al.*, *Fundamentals of heat and mass transfer*, vol. 6. Wiley New York, 1996.

[27] A. M. Elberry, J. Thakur, A. Santasalo-Aarnio, and M. Larmi, "Large-scale compressed hydrogen storage as part of renewable electricity storage systems," *International journal of hydrogen energy*, vol. 46, no. 29, pp. 15671–15690, 2021.

[28] H. L. Yip, A. Srna, A. C. Y. Yuen, S. Kook, R. A. Taylor, G. H. Yeoh, P. R. Medwell, and Q. N. Chan, "A review of hydrogen direct injection for internal combustion engines: Towards carbon-free combustion," *Applied Sciences (Switzerland)*, vol. 9, no. 22, 2019.

[29] Z. Stępień, "A comprehensive overview of hydrogen-fueled internal combustion engines: Achievements and future challenges," 2021.

[30] G. McTaggart-Cowan, K. Mann, J. Huang, A. Singh, B. Patychuk, Z. X. Zheng, and S. Munshi, "Direct Injection of Natural Gas at up to 600 Bar in a Pilot-Ignited Heavy-Duty Engine," *SAE International Journal of Engines*, vol. 8, no. 3, 2015.

[31] R. Caponi, A. M. Ferrario, E. Bocci, G. Valenti, and M. D. Pietra, "Thermodynamic modeling of hydrogen refueling for heavy-duty fuel cell buses and comparison with aggregated real data," *International Journal of Hydrogen Energy*, vol. 46, no. 35, 2021.

[32] I. Simonovski, D. Baraldi, D. Melideo, and B. Acosta-Iborra, "Thermal simulations of a hydrogen storage tank during fast filling," *International Journal of Hydrogen Energy*, vol. 40, no. 36, 2015.

A

Appendix 1

The analytical calculation of the 1st Law of Thermodynamics, leading to the expression presented in (2.1) is provided in this section, in (A.1).

$$\begin{aligned}
\frac{dU}{dt} = \frac{dH}{dt} - \frac{dQ}{dt} \Rightarrow \frac{du_g m_g}{dt} &= \frac{dh_g m_g}{dt} - \dot{Q} \Rightarrow \\
u_g \frac{dm_g}{dt} + m_g \frac{du_g}{dt} &= h_g \frac{dm_g}{dt} - \dot{Q} \Rightarrow \\
u_g \dot{m}_g + m_g \frac{d(c_v(T)T_g)}{dt} &= h_g \dot{m}_g - \dot{Q} \Rightarrow \\
c_v(T) m_g \frac{dT_g}{dt} &= (h_g - u_g)\dot{m}_g - \dot{Q} \Rightarrow \\
\frac{dT_g}{dt} &= \frac{1}{c_v(T) m_g}(\dot{m}_g p_g v_g - \dot{Q})
\end{aligned} \tag{A.1}$$

Some of the Simulink model shots are presented here for further insight in the structure and format of the model.

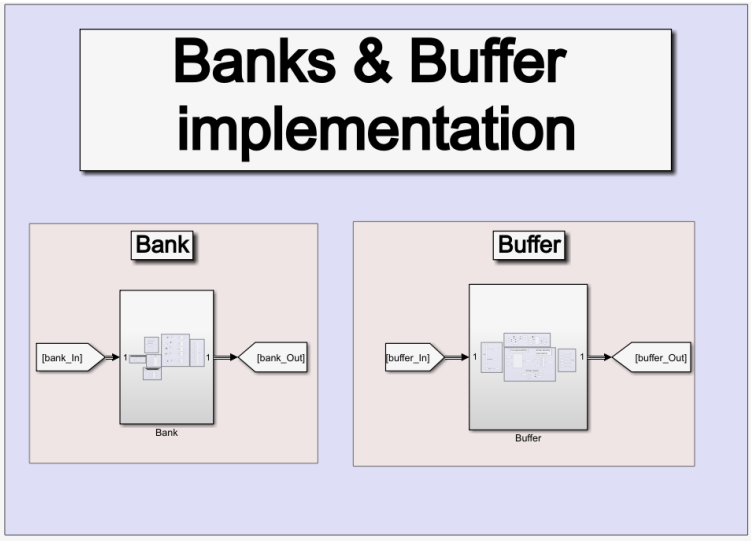

Figure A.1: Outside view of the Bank & Buffer blocks

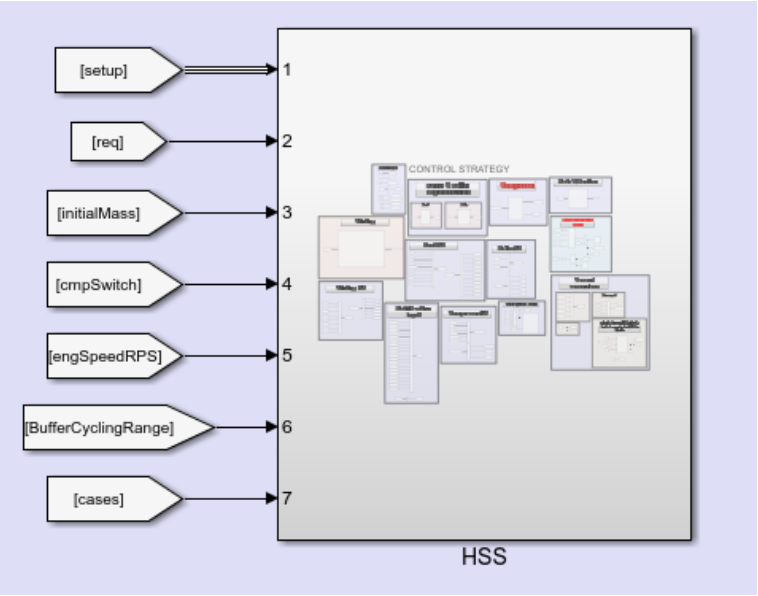

Figure A.2: Outside block view of the HSS

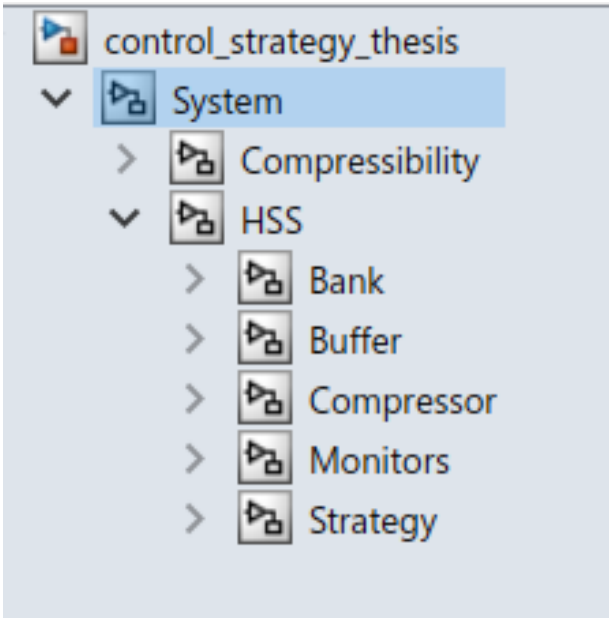

Figure A.3: The main menu structure

DEPARTMENT OF MECHANICS AND MARITIME SCIENCES
CHALMERS UNIVERSITY OF TECHNOLOGY
Göteborg, Sweden
www.chalmers.se

CHALMERS
UNIVERSITY OF TECHNOLOGY